

Abundances and Isotope Ratios in the Magellanic Clouds: The Star Forming Environment of N113⁶

M. Wang^{1,2}, Y.-N. Chin³, C. Henkel², J. B. Whiteoak⁴, M. Cunningham⁵

mwang@pmo.ac.cn

ABSTRACT

With the goal of deriving the physical and chemical conditions of star forming regions in the Large Magellanic Cloud (LMC), a spectral line survey of the prominent star forming region N113 is presented. The observations cover parts of the frequency range from 85 GHz to 357 GHz and include 63 molecular transitions from a total of 16 species, among them spectra of rare isotopologues. Maps of selected molecular lines as well as the 1.2 mm continuum distribution are also presented. Molecular abundances in the core of the complex are consistent with a photon dominated region (PDR) in a nitrogen deficient environment. While CO shows optical depths of order $\tau \sim 10$, ^{13}CO is optically thin. The most prominent lines of CS, HCN, and HCO^+ show signs of weak saturation ($\tau \sim 0.5$). Densities range from $5 \times 10^3 \text{ cm}^{-3}$ for CO to almost 10^6 for CS, HCN, and a few other species, indicating that only the densest regions provide sufficient shielding even for some of the most common species. An ortho- to para- H_2CO ratio of ~ 3 hints at H_2CO formation in a warm ($\gtrsim 40 \text{ K}$) environment. Isotope ratios are $^{12}\text{C}/^{13}\text{C} \sim 49 \pm 5$, $^{16}\text{O}/^{18}\text{O} \sim 2000 \pm 250$, $^{18}\text{O}/^{17}\text{O} \sim 1.7 \pm 0.2$ and $^{32}\text{S}/^{34}\text{S} \sim 15$. Agreement with data from other star forming clouds shows that the gas is well mixed in the LMC. The isotope ratios do not only differ from those seen in the Galaxy. They also do not form a continuation of the trends observed with decreasing metallicity

¹Purple Mountain Observatory, 2 West Beijing Road, 210008 Nanjing, China

²Max-Planck-Institut für Radioastronomie, Auf dem Hügel 69, D-53121 Bonn, Germany

³Department of Physics, Tamkang University, 251-37 Tamsui, Taipei County, Taiwan

⁴Australia Telescope National Facility, CSIRO Radiophysics Labs. P.O. Box 76, Epping, NSW 2121, Australia; vis. 1966 Coomba Rd, Coomba Park, NSW 2428, Australia

⁵School of Physics, University of New South Wales (UNSW), 2052 Sydney, Australia

⁶Based on observations with the Swedish/ESO Submillimeter Telescope (SEST) at the European Southern Observatory (ESO, La Silla, Chile) and the Atacama Pathfinder EXperiment (APEX, Chajnantor, Chile) of the Max-Planck-Institut für Radioastronomie (MPIfR), ESO, and Onsala Space Observatory (OSO)

from the inner to the outer Galaxy. This implies that the outer Galaxy, even though showing an intermediate metallicity, is not providing a transition zone between the inner Galaxy and the metal poor environment of the Magellanic Clouds. A part of this discrepancy is likely caused by differences in the age of the stellar populations in the outer Galaxy and the LMC. While, however, this scenario readily explains measured carbon and oxygen isotope ratios, nitrogen and sulfur still lack a self-consistent interpretation.

Subject headings: Galaxies: abundances – Galaxies: Magellanic Clouds – Galaxies: individual, LMC – Radio lines: galaxies – Radio continuum: galaxies

1. Introduction

The Magellanic Clouds are two southern irregular galaxies that provide unique opportunities to study astrophysical processes (e.g., Westerlund 1990). Noteworthy are their extremely small distances (~ 50 and 60 kpc), low heavy element contents, low dust-to-gas mass ratios, high $[\text{O}/\text{C}]$ and $[\text{O}/\text{N}]$ elemental abundance ratios, high atomic-to-molecular hydrogen (H/H_2) ratios, and an intense ultraviolet (UV) and far-ultraviolet (FUV) radiation field. The Magellanic Clouds, which are much smaller than the Milky Way, are characterized by a lower degree of nuclear processing than the Galaxy. Right now, however, they are undergoing an episode of vigorous star formation.

In the past couple of decades there have been an enormous number of studies of the Magellanic Clouds (see, e.g., the IAU Symposia No. 108, 148 190, and 256). The first systematic molecular surveys, covering the central parts of the Magellanic Clouds in the CO $J=1-0$ line were those of Cohen et al. (1988) and Rubio et al. (1991) with angular resolutions of $8''.8$. More detailed CO surveys were carried out with the NANTEN telescope at $2''.6$ resolution (e.g., Yamaguchi et al. 2001; Mizuno et al. 2006). CO data with even higher resolution, obtained in the $J=1-0$ and $2-1$ lines with $50''$ and $25''$ beamwidth, were taken with the SEST (Swedish-ESO Submillimeter Telescope). Several articles were published as part of the SEST Key-Program on CO in the Magellanic Clouds (e.g., Israel et al. 2003).

While these studies provide an overall view of the well shielded molecular medium in the Magellanic Clouds, multiline studies investigating the physical and chemical properties of the gas only exist for a very small number of targets in the vicinity of prominent HII regions. Following the pioneering study of Johansson et al. (1994) on N 159 in the LMC, Chin et al. (1997, 1998) and Heikkilä, et al. (1998, 1999) published molecular multi-line studies on star forming regions in the Magellanic Clouds. First detections of deuterated molecules outside

the Galaxy were reported by Chin et al. (1996b) and Heikkilä, et al. (1997).

N 113, located in the central part of the LMC more than 2° west of 30 Dor, is hosting the most intense H_2O maser of the Magellanic Clouds (Whiteoak & Gardner 1986; Lazendic et al. 2002; Oliveira et al. 2006). OH maser emission was also observed (Brooks & Whiteoak 1997). An IRAS (InfraRed Astronomy Satellite) point source, IRAS 0513–694, is associated with N 113. While Chin et al. (1996b, 1997) and Wong et al. (2006) collected single-dish and interferometric data from some $\lambda 3\text{ mm}$ transitions, a dedicated molecular multiline study of this star forming region covering the $\lambda 1\text{--}3\text{ mm}$ band is still missing. To improve our understanding of the interstellar medium (ISM) associated with massive star formation in an environment with low metallicity and to obtain a comprehensive view onto one of the most remarkable star forming regions of the LMC, we mapped the 1.2 mm continuum, obtained a spectral survey of the central region, and also mapped the cloud in several molecular lines.

2. Observations

2.1. 1.2 mm continuum observations

In October 2002 and August 2003 the 15-m SEST Imaging Bolometer Array SIMBA was used to image the distribution of continuum emission at 250 GHz ($\lambda 1.2\text{ mm}$) associated with N113. The 37-channel instrument was configured to map an area with dimensions of $400''$ in azimuth and $392''$ in elevation by means of 51 successive azimuth scans, at $80''/\text{sec}$, with a separation of $8''$ in elevation. Including overhead, a completed map took about six minutes. A total of 32 maps were obtained, 20 during the first observing period and 12 during the second.

At 250 GHz , the SEST beam had a full width to half maximum (FWHM) of $\sim 24''$. Accurate pointing and focus of the antenna were maintained with periodic observations of point-source calibrators (mainly OA 129). Periodic skydip observations provided estimates of the sky opacity. The derived zenith optical depths for both observing periods averaged about 0.14. Flux density calibration was provided by observations of Uranus, and were based on an adopted brightness temperature of 93 K for the planet.

The observations were processed using MOPSI, a software program developed and upgraded by R. Zylka (IRAM/Grenoble). Images were produced for each set of scans, and these were averaged to produce an image gridded in right ascension and declination. To reduce systematic baseline effects, the area containing the main source emission was defined by a polygon boundary, and this area was excluded from baselining corrections in a second averaging process. The algorithm PLANET enabled a flux density/beam scale to be derived

from the Uranus observations.

2.2. Spectroscopic measurements

2.2.1. SEST 15-m observations

With the SEST, observations were carried out in January and September 1995, January and March 1996, January, March, July, and September 1997, July 1998, and July 1999. For the frequency ranges, single-sideband system temperatures on a main beam brightness temperature scale (T_{mb}), beam widths and linear resolutions, see Table 1. 3 and 2 mm or 3 and 1.3 mm SIS receivers were employed simultaneously. For the SIS receiver used at 330–357 GHz, see also Mauersberger et al. (1996b).

The backend was an acousto-optical spectrometer (AOS) which was split into 2×1000 contiguous channels for simultaneous $\lambda \sim 3$ and 2 mm observations. At $\lambda \sim 1.3$ and 0.85 mm, all 2000 channels were used to cover a similar velocity range. The channel separation of 43 kHz corresponds to $0.04\text{--}0.15 \text{ km s}^{-1}$ for the frequency interval 357–85 GHz.

All measurements were made with a circular rotating disk to enable the beam to be either reflected or to pass through to a mirror system behind it. The two light beams allowed us to observe in a dual beam switching mode with a switching frequency of 6 Hz (controlled by the rotational speed of the disk) and a beam throw of $11'40''$ in azimuth. Since rapid beam switching was used in conjunction with reference positions on both sides of the source, baselines are of good quality. Calibration was obtained with the chopper wheel method. Main beam efficiencies of 0.746, 0.683, 0.457 and 0.30 at 94, 115, 230, and 345 GHz, respectively, were derived from measurements of Jupiter (L. Knee, priv. comm.; see also Table 1). These values were interpolated and, if necessary, also extrapolated to convert antenna (T_{A}^*) to main beam brightness (T_{mb}) temperature. The pointing accuracy, obtained from measurements of the nearby SiO maser source R Dor, was mostly better than $10''$ (see also Sect. 3).

2.2.2. APEX 12-m observations

In October 2007, observations of the CO $J=3\text{--}2$ line were carried out with the double sideband APEX-2a facility receiver (Risacher et al. 2006). 145 positions were measured in a position switching mode with an on-source integration time of 40 sec and a beamwidth of $\sim 20''$ (see Table 1). The beam efficiency was 0.73 and the forward hemisphere efficiency

0.97 (Güsten et al. 2006). Both units of a Fast Fourier Transform Spectrometer with 1 GHz bandwidth and 16384 channels each (Klein et al. 2006) were used to measure the CO transition. System temperatures on a T_A^* scale were 300–450 K.

3. Results

Figure 1 shows a 1.2 mm continuum map that is sensitive to the column density of the interstellar dust. Outside the core of N 113, which shows an elongation along an axis extending from the north-west to the south-east, we find protrusions toward the north and east, the latter only slightly surpassing the noise level. Figure 2 shows the corresponding distribution of integrated CO $J=3-2$ emission. While the morphology appears to be similar, the eastern tongue is detected with higher significance. The dashed outer contour still represents a 6σ level.

Figures 3–6 display the spectra measured toward the peak of N 113. Agreement between the APEX and SEST CO $J=3-2$ spectra at the central position is reasonably good (peak line temperatures are 10.5 and 12 K on a T_{mb} scale, respectively). SEST line parameters are given in Table 2 and include 50 detected, 7 tentatively detected, and 6 undetected transitions. The $^{12}\text{C}^{34}\text{S}$ $J=5-4$, $^{12}\text{C}^{33}\text{S}$ $3-2$, $^{13}\text{C}^{32}\text{S}$ $2-1$, and HC_3N $10-9$ spectral features show deviations from a radial velocity of $\sim 235 \text{ km s}^{-1}$. These are, however, likely caused by noise, as the emission in the above transitions is significantly weaker than in the other listed lines of CS. The relatively high velocity of the N_2H^+ $1-0$ transition (Table 2) may be a consequence of the presence of seven hyperfine components. Deviations from the relative intensities expected in the case of Local Thermodynamic Equilibrium (LTE) could shift the line by $\sim 1-2 \text{ km s}^{-1}$. Alternatively, an exceptional drift in the velocity scale of the temperature sensitive backend cannot be excluded. Among the 16 molecules observed (this includes 28 “isotopologues”, i.e. species containing different isotopic substitutions), only two remain undetected, NO and HCNO. Both contain nitrogen.

Also obtained were small maps in 10 molecular lines, including CO, ^{13}CO , and the higher density tracers CS, HCN, HCO^+ , and H_2CO . Observed positions and contour plots are displayed in Fig. 7. The maps outline to a certain degree the extent of the molecular cloud. Since its size is, however, often comparable to the size of the beam of the telescope, a deconvolution of the beam was necessary. The results of this deconvolution are given in Table 3. Shown are the transition (Cols. 1 and 2), the beam width (Col. 3), the observed Full Width to Half Power (FWHP) source size in right ascension and declination (Cols. 4 and 5), the deconvolved extent in right ascension and declination (Cols. 6 and 7) and its geometric mean (Col. 8). In view of map spacing and possible pointing errors, resulting

intrinsic source sizes are not accurate. Thus for CO $J=3-2$ SEST (Fig. 7) and APEX (Fig. 2) data deconvolved source sizes are 40 and 60'', respectively. For HCN, the intrinsic size of the emitting region remains undetermined, while the half power extent of the $\lambda 1.2$ mm continuum emission appears to be intermediate between those of CO $J=1-0$ and $2-1$ and the average value derived from the molecular high density tracers (see Sect. 4.2 for adopted source sizes).

4. Discussion

N 113 is with N 159 one of the two strongest molecular line emitters of the Magellanic Clouds. Prior to a detailed analysis of our spectra, some general source properties should be mentioned. From the IRAS flux densities (5.7, 40.5, 268, and 415 Jy at 12.5, 25, 60, and 100 μ m, respectively) we obtain a total luminosity of $\sim 2 \times 10^6 L_{\odot}$ for N 113, extrapolating from 6 to 400 μ m and assuming a grain emissivity proportional to ν (see Wouterloot & Walmsley 1986). Wong et al. (2006) collected $\lambda 3$ mm SEST, Mopra, and ATCA (Australia Telescope Compact Array) data of the radio continuum and prominent molecular species toward N 113. While the 3 mm continuum only reveals a flux density of ~ 40 mJy from a 5–10'' sized source (presumably, there is missing flux), their SEST HCN and HCO⁺ spectra toward the cloud core are consistent with our data. In agreement with our measurements (Fig. 7, Table 3), their SEST and Mopra maps also show a source that is only slightly more extended than the telescope beam. The interferometric high resolution ATCA maps did not collect the entire flux but reveal a compact cloud core of size 8'' \times 5'', with HCO⁺ $J=1-0$ being presumably more extended than HCN $J=1-0$.

In the following we first discuss the $\lambda 1.2$ mm continuum (Sect. 4.1) and then proceed to the analysis of spectral lines from individual molecular species (Sects. 4.2 and 4.3). Summaries of the observed properties with respect to H₂ densities (Sect. 4.4), molecular column densities (Sect. 4.5), and stellar nucleosynthesis (Sect. 4.6) follow.

4.1. The dust continuum

The 60 and 100 μ m IRAS fluxes and an emissivity proportional to ν yield a dust color temperature of $T_{d(60/100)} = 42.5$ K. With an integrated $\lambda 1.2$ mm flux density of 1.6 Jy (see Fig. 1) and an emissivity proportional to ν^2 we obtain a 100 μ m to 1.2 mm dust color temperature $T_{d(100/1200)} = 21$ K. The uncertainty in the 1.2 mm flux density of $\pm 20\%$ causes an error in T_{dust} that does not surpass ± 2 K. Applying the equation given in Table 3 of Mauersberger

et al. (1996a), we then obtain for dust temperatures between 20 to 45 K a total gas mass of $M_{\text{N113}} = (6.7 - 3.0) \times 10^5 M_{\odot}$. This assumes a dust to gas mass ratio of 500, which is a factor of four higher than in the solar neighborhood (Bolatto et al. 2000). For the 24'' sized central area (420 mJy), the column density becomes $(1.0 - 0.5) \times 10^{23} \text{ cm}^{-2}$ for the range of plausible dust temperatures (see Sect. 4.2.1 for the corresponding estimate from CO). The total mass estimated by us is a little larger than that given by Wong et al. (2006) who favored $M_{\text{N113}} \sim 10^5 M_{\odot}$.

4.2. Molecules with LVG modelling

With a Large Velocity Gradient (LVG) model (e.g., Sobolev 1960; Castor 1970; Scoville & Solomon 1974) and choosing a spherically symmetric cloud geometry, the H_2 density and the column density of a given species can be estimated. As input this requires some knowledge of the kinetic temperature as well as line intensities from a sufficient number of transitions of a given molecule. The choice of a particular cloud geometry can affect resulting densities by up to half an order of magnitude, but only if the lines are optically thick. Applying a plane-parallel instead of a spherical cloud geometry can result in particle densities which are lower by up to this amount.

We correct for beam dilution by calculating $T'_{\text{mb}} = T_{\text{mb}}/\eta_{\text{bf}}$ with $\eta_{\text{bf}} = \theta_s^2/(\theta_s^2 + \theta_b^2)$. θ_b and θ_s denote beam and source size, respectively (see also Wang et al. 2004). With the exception of a few CO lines (see Sect. 3) a source size of 40'' was assumed, which is consistent with the extent of the 1.2 mm continuum emission (Sect. 3, Fig. 1, and Table 3) and with the average of the (individually uncertain) molecular cloud size estimates of Table 3. Table 4 shows line temperatures prior and after correction for beam dilution.

The results of the model calculations that are based on the corrected line temperatures are shown in Figs. 8–13. Displayed are line intensities and peak line intensity ratios as a function of H_2 density and molecular column density.

In the following, LVG simulations are discussed for the most important molecular species. Calculations were made for kinetic temperatures of 20, 50, and 100 K (see e.g., Mangum & Wootten 1993, Chin et al. 1996b, and Heikkilä, et al. 1999 for a justification of the chosen temperature range).

4.2.1. CO

All of the eight lines of carbon monoxide (CO) shown in the left panels of Fig. 1 have been clearly detected. The lineshapes are compatible. While the $^{12}\text{C}^{17}\text{O}$ (hereafter C^{17}O) $J=1-0$ line is broader than all other measured CO transitions, this is not an effect caused by a relatively low signal-to-noise level. Hyperfine splitting, leading to two blended main spectral features separated by a few km s^{-1} (see Lovas & Krupenie 1974; Wouterloot et al. 2005), is broadening the line. A comparison of the $^{12}\text{C}^{18}\text{O}$ (hereafter C^{18}O) and C^{17}O $J=1-0$ lines results in an intensity ratio of 1.7 ± 0.2 which is extremely low compared with galactic values measured by Penzias (1981) and Wouterloot et al. (2005). The line intensity ratio agrees, however, with the average ratio of 1.6 ± 0.3 determined by Heikkilä et al. (1999) from the $J=2-1$ lines for a number of prominent HII regions of the LMC. As a consequence it is reasonable to assume that C^{18}O and C^{17}O are optically thin and that potential differences in shielding (Heikkilä et al. 1999) are minimal (see Sect. 4.6).

Because of optical depth effects, an interpretation of the $^{12}\text{C}^{16}\text{O}$ (hereafter CO) and $^{13}\text{C}^{16}\text{O}$ (hereafter ^{13}CO) spectra is less straightforward. With a $^{12}\text{C}/^{13}\text{C}$ isotope ratio of 49 ± 5 (Sect. 4.2.3) and $^{12}\text{CO}/^{13}\text{CO}$ line intensity ratios of 7.1, 4.8 and 3.5 for the $J=1-0$, $2-1$ and $3-2$ transitions, respectively (see Tables 2 and 5), CO opacities must be of order $\tau \sim 7$, 10, and 14. These are consistent with opacities of typical galactic clouds (e.g. Larson 1981), but are much larger than $\tau \sim 1$, which was proposed by Heikkilä et al. (1999) for the CO $J=1-0$ transition in other star forming regions of the LMC. For our estimate we have assumed that CO and ^{13}CO excitation temperatures are similar and that fractionation (Watson et al. 1976) and isotope selective photodissociation (Bally & Langer 1982) are either not important or are balancing each other. For the Galaxy, prominent molecular clouds do not show strong differences in the relative abundances of ^{12}C and ^{13}C bearing isotopologues (for CO, CN, and H_2CO , see Milam et al. 2005). For the LMC this is less clear (e.g., Heikkilä et al. 1999). In any case, the measured CO/ ^{13}CO line intensity ratios are large enough to ensure that ^{13}CO is optically thin. Larger opacities resulting in the observed smaller $^{12}\text{C}/^{13}\text{C}$ line intensity ratios in the higher- J rotational CO transitions are expected because of the higher statistical weights of the molecular states involved.

While $^{18}\text{O}/^{17}\text{O}$ and $^{12}\text{C}/^{13}\text{C}$ isotope ratios have previously been determined in several star forming regions of the LMC and while the gas appears to be well mixed, showing similar ratios in different sources (see Heikkilä et al. 1998 for the oxygen ratio), the higher and thus more elusive $^{16}\text{O}/^{18}\text{O}$ isotope ratio was so far only determined in N 159W (Heikkilä et al. 1999, their Table 16). With the $^{12}\text{C}/^{13}\text{C}$ isotope ratio directly obtained from the relative strengths of the HCN $J=1-0$ hyperfine components and the line intensity ratio of its ^{12}C and ^{13}C bearing species (Sect. 4.2.3 and Chin et al. 1999), a more accurate estimate is possible for

N 113. If $^{13}\text{CO } J=1-0$ is optically thin as indicated above, the $^{16}\text{O}/^{18}\text{O}$ ratio is determined by multiplying the $^{13}\text{CO}/\text{C}^{18}\text{O } J=1-0$ line intensity ratio by 49 ± 5 , which is the $^{12}\text{C}/^{13}\text{C}$ isotope ratio deduced from HCN (Sect. 4.2.3). We obtain $^{16}\text{O}/^{18}\text{O} = 2000\pm250$. This result is in good agreement with the value given in Table 16 of Heikkilä et al. (1999) for N 159W, suggesting that the ratio, like that of $^{18}\text{O}/^{17}\text{O}$, may not vary strongly from source to source. The $^{16}\text{O}/^{18}\text{O}$ value is four to ten times larger than corresponding ratios determined in the interstellar medium of spiral galaxies (e.g., Henkel & Mauersberger 1993). It yields a double isotope abundance ratio of $^{13}\text{CO}/\text{C}^{18}\text{O} \sim 40$, also consistent with the value proposed by Heikkilä et al. (1998) for N 159W. For $^{16}\text{O}/^{17}\text{O}$, we obtain 3400 ± 600 .

With ^{12}CO opacities of order 10, a carbon isotope ratio of ~ 50 , and the $^{16}\text{O}/^{18}\text{O}$ ratio determined above, ^{13}CO should be optically thin not only in the $J=1-0$, but also in the 2–1 and 3–2 transitions. Multiplying the ^{13}CO column density derived from LVG modeling by 50, taking collision rates with H_2 from Flower (2001), and assuming an ortho-to-para H_2 abundance ratio of 3:1 allows us to determine the total CO column density. With the LVG code we obtain $N(\text{CO}) \sim 6.5 \times 10^{17} \text{ cm}^{-2}$ and $n(\text{H}_2) \sim 5 \times 10^3 \text{ cm}^{-3}$. For a graphic display of the results that neither strongly depend on the choice of the collision rates nor on the ortho-to-para H_2 abundance ratio, see Fig. 7. The resulting values hold approximately for kinetic temperatures between 20 and 100 K.

Applying the mass estimate given by MacLaren et al. (1988) for a virialized cloud with an $1/r$ density gradient, we find for a cloud size of $R=5.5 \text{ pc}$ ($23''$, Table 1; this is within the range of beam radii listed in Table 3) and a linewidth of 5 km s^{-1} , $N(\text{H}_2) \sim 1.7 \times 10^{22} \text{ cm}^{-2}$, $N(\text{CO})/N(\text{H}_2) \sim 4 \times 10^{-5}$, and $\langle n(\text{H}_2) \rangle \sim 500 \text{ cm}^{-3}$. The CO/ H_2 abundance ratio is about half that characterizing galactic clouds (e.g., Frerking et al. 1982). The conversion factor between H_2 column density and CO $J=1-0$ integrated intensity becomes with $I_{\text{CO } 1-0} \sim 50 \text{ K km s}^{-1}$ (Table 2) $X = N(\text{H}_2)/I_{\text{CO } 1-0} \sim 3.4 \times 10^{20} \text{ cm}^{-2} (\text{K km s}^{-1})^{-1}$. This is almost twice the value for the galactic disk (e.g., Mauersberger et al. 1996a, their Appendix A.1) and the value reported by Chin et al. (1997) on the basis of a small number of CO lines observed toward N 113. Since uncertainties amount to at least a factor of two, our value is still consistent with approximately galactic values on small spatial scales, as already suggested by Rubio et al. (1993) and Chin et al. (1997) for the Magellanic Clouds. The column density derived for a virialized cloud is smaller than that obtained from the dust continuum in Sect. 4.1. This may in part be caused by the different beams considered. If most of the dust emission would arise from the compact core seen by Wong et al. (2006), we had to multiply the $N(\text{H}_2) = (5-10) \times 10^{22} \text{ cm}^{-2}$ from the dust emission by $(24''/45'')^2$, yielding column densities of $(1.4-2.8) \times 10^{22} \text{ cm}^{-2}$. This agrees well with the virial estimate from the CO data.

4.2.2. CS

Ten lines of carbon monosulfide (CS) were observed. The results are shown in the right two panels of Fig. 3 and in the left panel of Fig. 4. While the three lower- J lines of the main isotopic species, $^{12}\text{C}^{32}\text{S}$ (hereafter CS), are clearly seen, the $J=7-6$ line is only tentatively detected. The rare isotopologue $^{12}\text{C}^{34}\text{S}$ (hereafter C^{34}S) was detected in two and tentatively also in a third transition, while weak features are also seen at the frequencies of the $J=2-1$ and $3-2$ lines of $^{13}\text{C}^{32}\text{S}$ (hereafter ^{13}CS) and of the $J=3-2$ line of $^{12}\text{C}^{33}\text{S}$ (hereafter C^{33}S).

Are the lines of the main CS species optically thick, like those of CO? The $J=3-2$ transition, which is strongest, measured in four isotopologues, provides useful hints. For the CS/ ^{13}CS $J=3-2$ line intensity ratio we obtain 37 ± 5 , which is a little less than the $^{12}\text{C}/^{13}\text{C}$ isotope ratio of ~ 50 (Sect. 4.2.3). This implies that optical depths are not large, minimizing effects of isotope selective photodissociation. Deviations in the abundance ratio between the ^{12}C and ^{13}C bearing species of CS and HCN should also be small (Langer et al. 1984). Therefore neglecting these two effects, we obtain an optical depth $\tau \sim 0.65$ for the $J=3-2$ line of the main species, if CS and ^{13}CS excitation temperatures are similar. For CS/ C^{34}S $J=3-2$, the line intensity ratio is 11.3 ± 1.1 . This is about a factor of two lower than the abundance ratio measured towards N159W (Heikkilä et al. 1999; their Table 16), again suggesting a moderate degree of saturation in the CS $J=3-2$ line. With $\tau(\text{CS } 3-2) \sim 0.65$ as derived above, the $^{32}\text{S}/^{34}\text{S}$ sulfur isotope ratio becomes ~ 15 , slightly lower than values in the Galaxy (Chin et al. 1996a) and in N159W. If the tentatively detected C^{33}S $J=3-2$ line is really almost as strong as the ^{13}CS $J=3-2$ line, this would imply $^{32}\text{S}/^{33}\text{S} < 100$. This value is smaller than the ratio of 120–150 found in the solar system, the local interstellar medium, and the late-type carbon star IRC+10216 (Mauersberger et al. 2004).

Because C^{34}S is certainly optically thin and exhibits stronger lines than the other rare CS species, it is the isotopologue of choice to simulate CS excitation and to determine CS column density and H_2 density. LVG calculations (collision rates from Turner et al. 1992) yield, multiplying the C^{34}S column by a factor of 15, $N(\text{CS}) \sim 2.5 \times 10^{13} \text{ cm}^{-2}$ and $n(\text{H}_2) \sim 10^6 \text{ cm}^{-3}$ for kinetic temperatures between 20 and 100 K. With an H_2 density several orders of magnitude higher than that determined for CO, CS must trace a different kind of molecular gas.

4.2.3. HCN, HCO^+ and HNC

HCN is detected in the $J=1-0$ and $3-2$ transitions (Fig. 5) together with the rare isotopologues H^{13}CN and HC^{15}N , which were observed in the $J=1-0$ line, and DCN, which

was measured in the $J=2-1$ line. For earlier discussions of isotope ratios, see Chin et al. (1996b, 1999). Here we emphasize that the HCN $J=1-0$ line is sufficiently narrow to show its hyperfine (HF) structure, i.e. three components with relative intensities of 5:3:1 in the optically thin limit under conditions of Local Thermodynamical Equilibrium (LTE). The ratios actually observed are 3.64:2.34:1 (errors are of order 10%), indicating a moderate degree of saturation in its stronger HF components. Comparing the intensity ratio between the weakest HF component ($\tau \sim 0.12$, see Table 2 of Chin et al. 1999) and the H^{13}CN line and multiplying this by the factor $(5+3+1)=9$ yields a $^{12}\text{C}/^{13}\text{C}$ isotope ratio of 49 ± 5 . This is presumably the most accurate carbon isotope ratio determined for the LMC because we were able to derive the ratio from optically thin lines (see, e.g., Johansson et al. 1994; Chin et al. 1996b; Heikkilä et al. 1999 for consistent but less accurate determinations in other star forming regions of the LMC). According to Langer et al. (1984), the ratio from HCN may be somewhat higher than the overall carbon isotope ratio, but in the Galaxy, such differences are found to be negligible (Milam et al. 2005). The ratio is thus used throughout the article. For details on $^{14}\text{N}/^{15}\text{N}$ and D/H , see Chin et al. (1996b, 1999).

Application of an LVG code (Fig. 10; collision rates from Schöier et al. 2005) yields H_2 densities of 8×10^5 , 3×10^5 , and $1.6 \times 10^5 \text{ cm}^{-3}$ for kinetic temperatures of 20, 50, and 100 K. The column density is $N(\text{HCN}) \sim 6.3 \times 10^{12} \text{ cm}^{-2}$.

HCO^+ was detected in a total of five lines, in the $J=1-0$, 3-2 and 4-3 transitions of the main species, the $J=1-0$ transition of H^{13}CO^+ and the $J=2-1$ transition of DCO^+ (first and second panel of Fig. 5). For the $J=1-0$ $\text{HCO}^+/\text{H}^{13}\text{CO}^+$ line intensity ratio, we find 39 ± 5 , again suggesting a moderate optical depth of order 0.5 as in the case of the CS $J=3-2$ and HCN $J=1-0$ lines. LVG calculations (Fig. 11) indicate H_2 densities of 6×10^5 , 2.5×10^5 , and $1.6 \times 10^5 \text{ cm}^{-3}$ and a column density of order $4 \times 10^{12} \text{ cm}^{-2}$. Note that for $T_{\text{kin}} = 20 \text{ K}$, the $J=4-3/J=3-2$ line intensity ratio cannot be reproduced, possibly suggesting that the kinetic temperature of the gas is higher in this star forming region. This induces a high uncertainty in the density estimate for this low kinetic temperature.

Because a rare HNC isotopologue has not been observed, the optical depth of its $J=1-0$ lines remains undetermined. Nevertheless, because the line is weaker than those of HCN and HCO^+ , the assumption of optically thin emission appears to be reasonable. Physical parameters of HCN and HNC are quite similar but chemical properties differ strongly (e.g., Schilke et al. 1992; Aalto et al. 2002). In spite of this assuming similar spatial distributions and excitation conditions, we tentatively obtain a total molecular column density of $N(\text{HNC}) \sim 2.5 \times 10^{12} \text{ cm}^{-2}$.

4.2.4. H_2CO

At least five lines of formaldehyde (H_2CO) are seen (second and third panels of Fig. 4). Three belong with $K_a=1$ to the ortho-species (the hydrogen atoms have parallel spin), two to the para-species ($K_a=0$, antiparallel spin). A sixth line, also from para- H_2CO ($K_a = 2$) may have been tentatively detected and may serve as a tracer of kinetic temperature in future studies (Mühle et al. 2007). The rare isotopologue HDCO was searched for in two transitions but remains undetected. Our LVG calculations are based on collision rates of Green (1991) with He that were scaled upwards by a factor of 1.37 to approximate collisions with H_2 . Results are presented in Fig. 11. Including 41 para- and 40 ortho- H_2CO levels with molecular states up to 300 cm^{-1} above the ground state, the results are consistent with optically thin emission. The column density of ortho- H_2CO is about three times that of para- H_2CO . This result is independent of the assumed kinetic temperature ($20\text{ K} \leq T_{\text{kin}} \leq 100\text{ K}$; Fig. 11). Since the lines show signal-to-noise ratios of order 10, 1σ errors are small and ortho-to-para abundance ratios below 2.5 or above 3.5 can be excluded. The ratio agrees with that expected in the case of formaldehyde formation in a warm ($T_{\text{kin}} \gtrsim 40\text{ K}$) environment (e.g., Kahane et al. 1984; Dickens & Irvine 1999) and is not far off the value of 2.6, determined by Heikkilä et al. (1999) for N 159W. Densities vary between 10^5 and 10^6 cm^{-3} but are, for a given kinetic temperature, within the uncertainties the same for ortho- and para- H_2CO . This and similar linewidths (see Table 2) suggest that both formaldehyde species reside in the same volume.

While our LVG model results seem to agree with optically thin emission, we do not have detections of rare isotopic species to prove this. HDCO is weaker than the main species by a factor of $\gtrsim 30$ (3σ). This is below the level found in the cool environment of some low-mass protostellar cores (e.g., Roberts et al. 2002; Parise et al. 2006) but does not provide significant constraints, neither to the optical depths of the main species nor to the cosmic D/H ratio (see e.g., Chin et al. 1996b; Heikkilä et al. 1997; Gerin & Roueff 1999 for details). With the lines assumed to be optically thin, column densities become $N(\text{para-}H_2CO) \sim 4 \times 10^{12}\text{ cm}^{-2}$ and $N(\text{ortho-}H_2CO) \sim 1.2 \times 10^{13}\text{ cm}^{-2}$. These column densities do not strongly depend on the assumed kinetic temperature.

4.2.5. CH_3OH

Two $J=2-1$ and another two $3-2$ lines of methanol (CH_3OH) were detected (last panel of Fig. 6). This is the first time that the rotational multiplets of methanol have been resolved in an extragalactic source (cf. Henkel et al. 1987; Heikkilä et al. 1999). At kinetic temperatures of $T_{\text{kin}} = 50$ and 100 K , the measured profiles lead to $N(CH_3OH) \sim 1.0 \times 10^{13}\text{ cm}^{-2}$

and $n_{\text{H}_2} \sim 3.2 \times 10^4 \text{ cm}^{-3}$ assuming optically thin emission. At $T_{\text{kin}} = 20 \text{ K}$, the density is poorly determined and may become $> 10^5 \text{ cm}^{-3}$, while the column density is not significantly changed.

4.2.6. C_3H_2

Both detected lines of cyclic C_3H_2 (hereafter c- C_3H_2) belong to the ortho-species. Using an LVG code with collision rates from Chandra & Kegel (2000), we obtain densities of $n(\text{H}_2) = 3 \times 10^4$ and $9 \times 10^4 \text{ cm}^{-2}$ for $T_{\text{kin}} = 100$ and 25 K , respectively. The 1σ uncertainty in the deconvolved line ratio, 0.39 ± 0.08 (see Tables 2 and 4), which accounts for errors in the Gaussian fits, yields 1σ deviations in density by a factor of 2. The column density becomes $N(\text{c-C}_3\text{H}_2) \sim 3 \times 10^{12} \text{ cm}^{-2}$.

4.3. Other molecular species

4.3.1. CN

CN shows complex spectra. Each CN rotational state with $N > 0$ is split into a doublet by spin-rotation interaction. Because of the spin of the nitrogen nucleus, each of these components is further split into a triplet of hyperfine states. Calculated frequencies and relative intensities are given by Skatrud et al. (1983).

CN was detected in a total of 10 lines, seven belonging to the $1-0$ and three to the $2-1$ transition. Relative intensities of the detected $N=1-0$ features agree within 20% with the LTE predictions. When comparing its measured relative intensity with the corresponding LTE value, the strongest line ($J=3/2-1/2$, $F=5/2-3/2$; weight: $\sim 33\%$) is weaker than expected by almost 20%. For the two lines with the second largest LTE weights ($\sim 12\%$), such a discrepancy is not apparent. We conclude that all CN $N=1-0$ features are not highly saturated, with the strongest feature having an optical depth of $\tau \lesssim 0.5$.

The three $N=2-1$ observed transitions are also not providing evidence for high opacities. Here the line with intermediate intensity ($J=3/2-1/2$, $F=5/2-3/2$) is much weaker than expected. LTE ratios are 26.7:16.7:6.1, which should be compared with observed ratios of 31.5:10.6:7.4 (errors are of order 10–15%).

In the optically thin limit, the CN excitation temperature can be obtained from the

ratio between the sum of the $N=2-1$ and $1-0$ intensities using

$$R_{21} = 4 \times e^{-x} \times \frac{1 - e^{-2x}}{1 - e^{-x}} \times \frac{(e^{2x} - 1)^{-1} - (e^{2y} - 1)^{-1}}{(e^x - 1)^{-1} - (e^y - 1)^{-1}},$$

with $x = h\nu_{10}/kT_{\text{ex}}$, $y = h\nu_{10}/(k \times 2.73)$ and $\nu_{10} = 113.386$ GHz (see Wang et al. 2004). While the integrated intensity of the $N=1-0$ transition is well determined (only two components representing together $\sim 2.5\%$ of the total LTE intensity are not observed), the three measured $N=2-1$ features only provide $\sim 50\%$ of the total intensity under LTE conditions. Thus the total $N=2-1$ intensity in R_{21} is less well determined and, in view of potential deviations from LTE conditions, an error cannot be derived. Ignoring these uncertainties and accounting for the LTE intensities of the unobserved features, we obtain a line intensity ratio of 1.20. Correcting for the different beam sizes at 3 and 1.3 mm yields $R_{21} = 0.69$ and $T_{\text{ex}} = 5.6$ K. This value is small, indicating subthermal excitation (see e.g., Fuente et al. 1995). The column density becomes $N(\text{CN}) \sim 3.5 \times 10^{13} \text{ cm}^{-2}$.

4.3.2. Other molecules

The remaining molecular species are seen in too few transitions and do not provide enough information for a reliable estimate of density and excitation. Assuming, however, that the lines are optically thin (a realistic assumption, see Sects. 4.2.2, 4.2.3, and 4.3.1) and realizing that the column densities are almost independent of the chosen kinetic temperature, column densities can still be estimated in some cases. This involves an educated guess of the density.

We detected strong **SO** emission in the 4_3-3_2 transition (Fig. 6). The column density (Table 5) was calculated with an LVG code (70 levels up to 580 K above the ground state; collision rates from Green 1994) for $T_{\text{kin}} = 50$ K and $n(\text{H}_2) = 5 \times 10^4$ and $5 \times 10^5 \text{ cm}^{-3}$. The resulting column density becomes $1.5^{+1.5}_{-0.8} \times 10^{13} \text{ cm}^{-2}$.

Having observed two of the hyperfine components of the $N=1-0$ transition of **C₂H**, we find that their line intensity ratio, 2.4 ± 0.4 , is consistent with 2.0, the expected value for optically thin emission under LTE conditions. **C₂H** is present in UV irradiated molecular clouds as well as in well shielded cores (e.g., Pety et al. 2005; Beuther et al. 2008). Only having detected the $N=1-0$ transition, and with no LVG code at hand, a reliable column density could not be estimated (with the assumptions used by Wang et al (2004) for NGC 4945, the source averaged 5σ upper limit would become $7 \times 10^{14} \text{ cm}^{-2}$).

N₂H⁺ was detected in the $J=1-0$ line (Fig. 4). Individual hyperfine components are, unlike those of **HCN** $J=1-0$, blended. For the column density (Table 5) an LVG code was

used with 31 levels up to 2100 K above the ground state (collision rates from Schöier et al. 2005). With the parameters also used for SO, a column density of $7_{-1}^{+1} \times 10^{11} \text{ cm}^{-3}$ was calculated.

For **SO₂**, detected in the $5_{1,6}-4_{0,4}$ line, we used RADEX, an LVG code also calculating the radiative transfer for a homogeneous, isothermal sphere with high velocity gradient (van der Tak et al. 2007). The column density becomes $5_{-1}^{+1} \times 10^{12} \text{ cm}^{-2}$.

HC₃N was tentatively detected in the $J=10-9$ and $16-15$ transitions (Fig. 5). An LVG fit to the deconvolved brightness temperatures (22 levels up to 92 K above the ground state; collision rates from Green & Chapman 1978) yields for the determined upper limits and $T_{\text{kin}} = 50$ and 100 K densities of $n(\text{H}_2) \sim 3 \times 10^5 \text{ cm}^{-3}$ and $1.5 \times 10^5 \text{ cm}^{-3}$, respectively. $N(\text{HC}_3\text{N}) \lesssim 6 \times 10^{11} \text{ cm}^{-2}$ (Table 5). A kinetic temperature of 20 K is too small to fit the two tentatively detected lines.

Adopting the excitation conditions assumed by Martín et al. (2006) for NGC 253, NO and HNC source averaged 5σ upper limits to the column density would become $6.5 \times 10^{14} \text{ cm}^{-2}$ and $2.6 \times 10^{13} \text{ cm}^{-2}$, respectively.

4.4. Densities and chemical implications

The determination of spatial densities depends to a certain degree on the assumed kinetic temperature. Nevertheless, Table 5 clearly shows that the molecular species analyzed in some detail emit from regions that are characterized by three different density regimes. CO traces, not unexpectedly, the lowest density component, C₃H₂ and CH₃OH originate from gas with intermediate density. All the other molecules detected in more than one line trace the high density component that can only occupy a small volume because it is three orders of magnitude denser than the $\langle n(\text{H}_2) \rangle$ value derived for the inner 45'' of the cloud (Sect. 4.2.1).

CO, the studied species with by far the highest column density, has a natural advantage with respect to self-shielding in a hostile interstellar environment like that of the LMC (see Sect. 1). Furthermore, a small dipole moment leads to a particularly low “critical density”. Therefore collisional excitation to T_{ex} values well above the level of the cosmic microwave background is reached at comparatively low H₂ densities.

Cyclic C₃H₂ is a well known tracer of diffuse gas (e.g., Thaddeus et al. 1985; Cox et al. 1988) so that a lower density than for other species with a similarly high dipole moment is consistent with measurements of galactic clouds. However, such a similarity is not self-

evident. UV photons that are abundant in the LMC (e.g., Israel et al. 1996) might destroy all $c\text{-C}_3\text{H}_2$ except in the densest regions. That this is not the case is an important finding.

Quasi-thermal methanol (CH_3OH) has been observed to be sandwiched between shocked regions, seen in vibrationally excited H_2 , and CS, tracing the dense ambient medium (Liechti & Walmsley 1997; see also Table 5). Fractional methanol abundances can vary over several orders of magnitude (e.g., Kalenskii et al. 1997) and are sometimes drastically enhanced by grain mantle evaporation so that we may see emission arising preferentially from the outer, less dense, highly UV irradiated edges of the molecular complex.

CS, HCN, HCO^+ , and H_2CO trace the dense medium of N 113, but we should note that the CS, HCN, and HCO^+ $J = 1\text{-}0$ lines are slightly too strong for an optimal LVG fit. This suggests that some of their emission is also arising from the component with intermediate density. The $J=1\text{-}0$ line of para- H_2CO is not part of the 3 mm band and was therefore not observed. In galactic clouds HCO^+ often arises from lower density gas than HCN (e.g., Baan et al. 2008). Toward N 113, we do not see this effect, which may imply that HCN and HCO^+ are efficiently destroyed by photodissociation in the lower density parts of the cloud. There is some evidence that H_2CO may be related to photon dominated regions, i.e. to the lower density edges of molecular clouds that are irradiated by UV-photons. Toward M 82, another small galaxy with an intense UV field, Weiß et al. (2001) observed NH_3 and found that its emission must arise from relatively cool cloud cores that show a temperature similar to the overall dust radiation ($T_{\text{kin}} \sim 50\text{ K}$). H_2CO , however, was found to trace a much warmer gas component, with $T_{\text{kin}} \sim 200\text{ K}$ and a surprisingly low density, $n(\text{H}_2) \sim 7 \times 10^3\text{ cm}^{-3}$ (Mühle et al. 2007). In M 82, H_2CO may be related to evaporated dust grain mantles (e.g., Ceccarelli et al. 2001), but apparently this scenario does not hold for N 113.

Overall, the densities obtained for CO and the higher density tracers are within the range estimated by Heikkilä et al. (1999) for a number of other star forming clouds in the LMC. The exception is HCO^+ , which, in N 113, traces H_2 densities similar to those derived from HCN and CS, while Heikkilä report lower H_2 densities. The high H_2 density obtained by us is a surprise in view of the relatively large HCO^+ emission region that was suggested by Wong et al. (2006; see our Sect. 4) for N 113 and by Heikkilä et al. (1999) for other clouds in the LMC. It is possible, that only the HCO^+ $J=1\text{-}0$ line originates from a relatively large volume, while the $J=3\text{-}2$ transition (see Fig. 5) is solely tracing gas from the densest regions.

4.5. Column densities and chemical implications

To derive the fractional abundances in Tables 6 and 7 from the column densities given in Table 5, a reference is needed, which introduces an additional uncertainty. To minimize this error, we refer not to $N(\text{H}_2)$ but provide fractional abundances relative to $N(\text{CO})$. $N(\text{CO})$ has been analyzed in detail in Sect. 4.2.1. What peculiarities can be expected? The strongest deviations of abundances from galactic values may be related to nitrogen. Nitrogen is a predominantly “secondary” element. Being mainly synthesized on pre-existing carbon from a previous stellar generation, N underabundances are particularly large in regions having undergone little nuclear processing (e.g., Wheeler et al. 1989). B stars in the LMC show this effect. Observed are underabundances of C, N, and O by factors of ~ 5 , 10, and 2 relative to the solar system (e.g., Hunter et al. 2007).

The underabundance of N relative to C (i.e., CO) amounts to a factor of two. In view of the uncertainties mentioned above, this is close to the limit of what we can detect. Nevertheless, there are indications that this underabundance really plays a role. The two undetected species mentioned in Sect. 3 (NO and HCNO) are both nitrogen bearing. Considering the spectral range between 150 and 154 GHz, $\text{H}_2\text{CO}/\text{HNCO}$ and $\text{H}_2\text{CO}/\text{NO}$ line ratios are >15 and >20 versus ~ 2.1 and ~ 3.0 in NGC 253 (see Martín et al. 2006). For N 113, we also find (Table 5) $N(\text{CS}, \text{SO}, \text{H}_2\text{CO}, \text{CH}_3\text{OH}) > N(\text{HCN}, \text{HNC}, \text{N}_2\text{H}^+, \text{HC}_3\text{N})$, which is not typical for clouds outside the Magellanic Clouds (Tables 6 and 7).

Tables 6–7 show that in N 113 HCN and HC_3N are clearly underabundant, relative to CO, with respect to galactic as well as extragalactic molecular clouds (N 159 belongs like N 113 to the LMC and shows a similar trend). The case for HNC is not as strong, but our HNC abundance is based on a single line only. It may seem surprising that the one species with two nitrogen atoms, N_2H^+ , appears to be, relative to CO, as abundant as in galactic cores and in the nuclear regions of large spiral galaxies (Tables 6 and 7). This may be explained by the fact that N_2H^+ is a tracer of dense cores. It is not as easily depleted in a very dense ($n(\text{H}_2) \sim 10^6 \text{ cm}^{-3}$) medium as CO and most other species (e.g., Fontani et al. 2006). In the LMC, where only cloud cores may be visible in a variety of molecules because of an otherwise insufficient shielding by dust grains, a low nitrogen abundance might thus be complemented by a source averaged CO depletion of about the same amount, yielding an overall “galactic” $\text{N}_2\text{H}^+/\text{CO}$ abundance ratio. We have to emphasize, however, that this result requires confirmation, because it is based on a single molecular N_2H^+ transition with undetermined optical depth.

To avoid as much as possible complications caused by uncommon elemental abundances, relative column densities of isomers (e.g., HCN versus HNC) and of hydrogenated or protonated molecules (e.g., CN versus HCN, CO versus HCO^+ and H_2CO) are most suitable to

classify the molecular complex in terms of properties observed in more metal-rich galactic molecular clouds. Notable is the high abundance of the cyanide radical CN relative to HCN and HNC. The former is to a large extent a photodissociation product of the latter two molecules. The high CN abundance is thus likely caused by the strong UV radiation field in the LMC (see, e.g., Fuente et al. 2006 for the related case of the starburst galaxy M82).

An $N(\text{HCN})/N(\text{HNC})$ ratio larger than unity also favors the PDR scenario, which is further supported by $8\mu\text{m}$ emission attributed to polycyclic aromatic hydrocarbons (PAHs; see Wong et al. 2006) and by a lack of dust. As already mentioned (Sect. 4.1), the LMC requires for a given visual extinction about four times larger columns than the solar neighborhood (Bolatto et al. 2000). This allows UV radiation to penetrate deeper into the cloud. Associated with N113 are HD 269219, a $\sim 30 M_{\odot}$ supergiant B star, HD 269217, an emission line star, and a number of O9 to B0.5 stars either on the main sequence or slightly more evolved (Wilcots 1994; Oliveira et al. 2006). Table 6 presents fractional molecular abundances of a prototypical PDR, the Orion Bar.

Following Heikkilä et al. (1999), $N(\text{HC}_3\text{N})/N(\text{CN}) < 0.1$ is also indicative of a PDR. For N113 we find $\lesssim 0.2$ so that in this case the result is inconclusive. The CO/HCO^+ and $^{13}\text{CO}/\text{HCO}^+$ $J=1-0$ line intensity ratios, taken by Heikkilä et al. (1999) as an inverse measure of star forming and PDR activity (their Table 11), are with 13.8 ± 0.4 and 1.7 ± 0.1 a little higher than those of most other massive star forming regions of the LMC. This suggests that PDR activity may be less pronounced in N113. This and the prominent masers (Sect. 1) associated with the molecular complex may indicate that massive star formation has been triggered more recently in N113 than in most other active cores of the LMC.

Aside from N113 (see also Chin et al. 1997; Wong et al. 2006) N159 is the most thoroughly studied molecular complex of the LMC (e.g., Heikkilä et al. 1999). Table 7 compares column densities of several key molecules relative to $N(\text{CO})$. Overall, nitrogen deficiencies may be similar in N159 and N113.

M82 is an irregular galaxy of similar size as the LMC, but it hosts a starburst in its final stage. Accordingly, metallicities are higher than in the LMC (e.g., Origlia et al. 2004). NGC 253 and NGC 4945 are, on the other hand, large spirals with starburst activity in their nuclear regions. Table 7 therefore shows, from left to right, clouds with increasing metallicity. Increasing column densities w.r.t. CO are found for HCN, HCO^+ , and HNC between Col. 2 (N113) and Cols. 5 and 6 (NGC 253 and NGC 4945). For the nitrogen bearing species this is readily explained by the nitrogen deficiency of clouds in the smaller galaxies. It is not clear, however, why HCO^+ is following this trend. There are only small differences in the column densities of CS, H_2CO , and SO relative to those of CO. Considering CS/CO, sulfur and oxygen are both synthesized in massive stars. H_2CO and CO are both CO bearing.

The $N(\text{SO})/N(\text{CO})$ ratio is less trivial because at least some of the carbon is, unlike sulfur, synthesized in stars of intermediate mass. However, this may affect abundances much less than the more notable underabundance of nitrogen.

4.6. Isotope ratios

Optically, it is difficult to discriminate between isotopes of a given element, since their atomic lines are blended. However, spectra from a given molecular species containing different isotopic constituents, so-called “isotopologues”, are well separated, typically by a few percent of the rest frequency. This implies that blending is no problem, while frequencies are still close enough to be observed with the same technical equipment.

The hyperfine structure of the HCN $J = 1-0$ line allows us to determine the optical depth of each component and to obtain accurate $^{12}\text{C}/^{13}\text{C}$, $^{14}\text{N}/^{15}\text{N}$ and D/H ratios (for the latter, see Chin et al. 1996b; Heikkilä et al. 1997). CO provides $^{18}\text{O}/^{17}\text{O}$ and even $^{16}\text{O}/^{18}\text{O}$ ratios from optically thin lines, while CS offers opportunities to study sulfur isotopes.

Results are summarized in Table 8. There are three major findings: (1) *The ISM of the LMC is well mixed*, (2) *the ratios are very different from the corresponding galactic values*, and (3) *the carbon, nitrogen, and oxygen ratios demonstrate that the outer Galaxy is not providing an interstellar medium that is intermediate between that of the solar neighborhood and the LMC*.

With respect to mixing, the $^{18}\text{O}/^{17}\text{O}$ ratio is particularly noteworthy because it has been determined in the most direct way. Values of ~ 1.6 , much lower than in the Galaxy, are measured in prominent star forming regions throughout the LMC (Heikkilä et al. 1998). This does not only indicate that the gas is quite homogeneous in its composition, but also excludes effects of isotope selective fractionation, significant differences in shielding against UV radiation, and C^{17}O line intensities that are strongly influenced by non-LTE effects. Any one of these might produce a notable scatter in the ratios, but this is not observed.

The result that the ISM of the outer Galaxy does not provide a direct connection between the solar neighborhood and the LMC, was already addressed in the special case of $^{18}\text{O}/^{17}\text{O}$ ratios by Wouterloot et al. (2008) but deserves additional discussion. Wouterloot et al. suggested on the basis of four ratios from the outer Galaxy (galactocentric radii $16 \text{ kpc} \leq R_{\text{GC}} \leq 17 \text{ kpc}$; solar radius $R_{\odot} = 8.5 \text{ kpc}$) an interpretation in terms of current models of galacto-chemical evolution. Within the framework of “biased-infall” (e.g., Chiappini & Matteucci 1999), the galactic disk is slowly formed from inside out which is causing gradients in the abundances across the disk. The average ratio appears to be ~ 5 in the outer disk

but is only 1.6 in the LMC. In spite of the fact that the outer disk $^{18}\text{O}/^{17}\text{O}$ data are not numerous and uncertainties are large, the difference is far too large not to be significant. It is inconsistent with a pure metallicity dependence that was proposed by Heikkilä et al. (1998). It also does not indicate a lack of high mass stars as suggested by Heikkilä et al. (1999), since massive stars are numerous in the LMC (e.g., Westerlund 1990). The high ratio of the outer Galaxy was qualitatively interpreted in terms of a lack of ^{17}O , that is synthesized in largest quantities in stars of intermediate mass. Their ejecta, reaching the ISM with a time delay, are less dominant in the young stellar disk of the outer Galaxy than in the older stellar body of the LMC (Wouterloot et al. 2008; see, e.g., Hodge 1989 for the star formation history of the LMC). This interpretation is also consistent with the extremely high $^{18}\text{O}/^{17}\text{O}$ ratios (>10) obtained by Combes & Wiklind (1995) and Muller et al. (2006) toward the presumably young spiral arms of galaxies seen at redshifts of $z \sim 0.7$ and 0.9 .

The carbon ratio offers another test of this scenario, also indicating a well mixed interstellar medium in the LMC (see Sect. 4.2.3). For $^{12}\text{C}/^{13}\text{C}$, the galactic data base is particularly large. ^{13}C is like ^{17}O a secondary nucleus and should be underabundant relative to ^{12}C in the outer Galaxy, both with respect to the solar neighborhood and the LMC. This is indeed the case (Table 8). $^{12}\text{C}/^{13}\text{C}$ ratios are like $^{18}\text{O}/^{17}\text{O}$ highest in the outer Galaxy, smaller near the solar circle and smallest in the LMC. Also the solar system $^{12}\text{C}/^{13}\text{C}$ ratio is, like the $^{18}\text{O}/^{17}\text{O}$ ratio, higher than in the local interstellar medium. This is consistent with an infusion of material from massive stars into the early solar system and/or an enrichment of the local ISM by secondary nuclei during the past 4.6×10^9 yr.

Less conclusive is the nitrogen ratio. Ratios from beyond the Perseus arm ($R_{\text{GC}} > 10$ kpc) have not yet been reported. However, all galactic studies of elemental abundances or isotope ratios extending to large radii show no signs for a change in radial abundance gradients. If this also holds for $^{14}\text{N}/^{15}\text{N}$, then we face again a situation with highest ratios in the outer Galaxy, smaller ones near the solar system and smallest values in the LMC. The interpretation would then be, like those for $^{18}\text{O}/^{17}\text{O}$ and $^{12}\text{C}/^{13}\text{C}$, that ^{15}N is secondary with respect to the main ^{14}N species. This, however, is in conflict with a low $^{14}\text{N}/^{15}\text{N}$ ratio in the starburst galaxy NGC 4945 which suggests that ^{15}N is a nucleus mainly synthesized in massive stars due to rotationally induced mixing of protons into the helium-burning shells of massive stars (Chin et al. 1999). In view of this, there are two alternatives: (1) Either the weak HC^{15}N profile presented by Chin et al. for NGC 4945 is spurious and ^{15}N is predominantly synthesized in lower mass stars than ^{14}N or (2) the weak $^{14}\text{N}/^{15}\text{N}$ gradient presented by Wilson & Rood (1994) is not significant and ^{15}N is mainly a product of massive stars. There are three arguments supporting the latter view. These are (1) the low solar $^{14}\text{N}/^{15}\text{N}$ ratio (Table 8) that may be understood in terms of the above mentioned infusion of ejecta from massive stars, favoring ^{15}N , into the early solar system and/or enrichment of

the local ISM by secondary nuclei (i.e., ^{14}N) during the last 4.6×10^9 yr; (2) an extremely high $^{14}\text{N}/^{15}\text{N}$ ratio (>600 ; Wilson & Rood 1994) in the ISM of the galactic center region that is dominated by products of CNO burning, mainly from stars of intermediate mass; (3) the likely low nitrogen isotope ratio in the young lensing galaxy of the PKS 1830–211 system at redshift $z \sim 0.9$ (Muller et al. 2006). In case that the reported $^{14}\text{N}/^{15}\text{N}$ galactic disk gradient is real, however, more complex interpretations will be required. Obviously, interstellar $^{14}\text{N}/^{15}\text{N}$ ratios are not fully understood and more observational constraints are urgently needed.

Unlike $^{18}\text{O}/^{17}\text{O}$, $^{16}\text{O}/^{18}\text{O}$ appears to be an excellent tracer of metallicity. ^{16}O and ^{18}O are both products of helium burning with metal poor stars apparently ejecting little ^{18}O . Highest $^{16}\text{O}/^{18}\text{O}$ ratios are therefore found in the LMC (Table 8), lowest ratios in the galactic center region. The entire range of observed interstellar values covers almost an order of magnitude and would likely surpass it, if C^{18}O could be detected in the Small Magellanic Cloud.

Chin et al. (1996a) reported a strong positive gradient with galactocentric distance for $^{32}\text{S}/^{34}\text{S}$, which was a surprise because both nuclei are synthesized by oxygen burning in massive stars. The LMC ratio (Sect. 4.2.2 and Table 8) is substantially lower than those encountered in the local ISM and the solar system. Overall the situation seems to resemble that of the $^{14}\text{N}/^{15}\text{N}$ ratio (a reported positive gradient in the galactic disk, a solar system ratio that is smaller than in the local ISM, and an LMC ratio that is smaller than ratios measured in the Galaxy) and thus provides a strong motivation for more detailed observational studies to constrain models of high mass stellar evolution.

5. Conclusions

Toward the prominent star-forming region N 113 in the Large Magellanic Cloud, we obtained with the SEST a map of the $\lambda 1.2$ mm dust continuum as well as spectral line data covering 63 transitions from a total of 16 molecular species. These include 50 detections, 7 tentative detections, and 6 undetected transitions. The APEX and SEST telescopes also contribute molecular line maps.

(1) The total mass of the N 113 molecular complex is estimated to be a few $10^5 M_\odot$ with column densities of $N(\text{H}_2) \sim 2\text{--}10 \times 10^{22} \text{ cm}^{-2}$ for the central $45''$ (11 pc) and $24''$ (5.5 pc), respectively. Assuming virial equilibrium, we obtain for a $45''$ beam a $N(\text{CO})/N(\text{H}_2)$ abundance ratio of about 4×10^{-5} and a conversion factor of $X = N(\text{H}_2)/I_{\text{CO}1-0} = 3.4 \times 10^{20} \text{ cm}^{-2} (\text{K km s}^{-1})^{-1}$.

(2) The virial theorem suggests an average density of $n(\text{H}_2) \sim 500 \text{ cm}^{-3}$ for the central

45'' of the cloud. From CO we obtain a density of $n(\text{H}_2) \sim 5000$, for C_3H_2 and CH_3OH the density becomes several 10^4 cm^{-3} , while other molecular species (CS , HCN , HCO^+ , and H_2CO) mainly trace a gas density of several 10^5 cm^{-3} . This indicates a high degree of clumping. Efficient shielding for most of the molecular species seems to occur in the densest regions only.

(3) Among the molecular species observed, only two remain undetected, NO and HNC. HC_3N is only tentatively detected. All these molecules are nitrogen bearing. Chemically, the N 113 molecular complex can be described by a photon dominated region in an environment that lacks nitrogen. An ortho- to para- H_2CO column density ratio of ~ 3 indicates that at least formaldehyde was formed in a warm ($T_{\text{kin}} \gtrsim 40 \text{ K}$) medium.

(4) Comparing isotope ratios with line intensity ratios we find that CO is optically thick ($\tau \sim 10$), while ^{13}CO is optically thin. The main lines of CS, HCN, and HCO^+ are only moderately opaque ($\tau \sim 0.5$).

(5) The interstellar medium of the LMC appears to be well mixed. Carbon, nitrogen, and oxygen isotope ratios demonstrate that the outer Galaxy does not provide a “bridge” between the interstellar medium of the solar neighborhood and that of the LMC. This is likely caused by the high age of the stellar population of the LMC relative to that of the outer Galaxy. Adopting this scenario, observed carbon and oxygen isotope ratios are qualitatively understood, while nitrogen and sulfur isotope ratios remain an enigma.

We wish to thank S. Leurini for the use of her CH_3OH LVG code with collision rates provided by D. Flower, M. Rubio for useful discussions, and an anonymous referee for critically reading the manuscript. M. W. acknowledges support by the exchange program between the Chinese Academy of Sciences and the Max-Planck-Gesellschaft, and partly by grants 10733030 and 10621303 from NSFC and 2007CB815406 from MSTC. Y.-N. C. thanks for financial support by the National Science Council under NSC91-2112-M-032-013. J. B. W. and M. C. acknowledge the financial support supplied by the Australian Government’s Access to Major Research Facilities Program (AMRFP) for travel to the SEST.

REFERENCES

- Aalto, S., Polatidis, A. G., Hüttemeister, S., & Curran, S. J. 2002, *A&A*, 381, 783
- Baan, W. A., Henkel, C., Loenen, A. F., Baudry, A., & Wiklind, T. 2008, *A&A*, 477, 747
- Bally, J., & Langer, W. D. 1982, *ApJ*, 255, 143

- Beuther, H., Semenov, D., Henning, T., & Linz, H. 2008, *A&A*, 675, L33
- Blake, G. A., Sutton, E. C., Masson, C. R., & Phillips, T. G. 1987, *ApJ*, 315, 621
- Bolatto, A. D., Jackson, J. M., Israel, F., Zhang, X., & Kim, S. 2000, *ApJ*, 545, 234
- Brooks, K. J., & Whiteoak, J. B. 1997, *MNRAS*, 291, 395
- Castor, J. I. 1970, *MNRAS*, 149, 111
- Ceccarelli, C., Loinard, L., Castets, A., Tielens, A. G. G. M., Caux, E., Lefloch, B., & Vastel, C. 2001, *A&A*, 372, 998
- Chandra, S., & Kegel, W. H. 2000, *A&AS*, 142, 113
- Chiappini, C., & Matteucci, F. 1999, *ApS&S*, 265, 425
- Chin, Y.-N., Henkel, C., Whiteoak, J. B., Langer, N., & Churchwell, E. B. 1996a, *A&A*, 305, 960
- Chin, Y.-N., Henkel, C., Millar, T. J., Whiteoak, J. B., & Mauersberger, R. 1996b, *A&A*, 312, L33
- Chin, Y.-N., Henkel, C., Whiteoak, J. B., Millar, T. J., Hunt, M. R., & Lemme, C. 1997, *A&A*, 317, 548
- Chin, Y.-N., Henkel, C., Millar, T. J., Whiteoak, J. B., & Marx-Zimmer, M. 1998, *A&A*, 330, 901
- Chin, Y.-N., Henkel, C., Langer, N., & Mauersberger, R. 1999, *ApJ*, 512, L143
- Cohen, R. S., Dame, T. M., Garay, G., Montani, J., Rubio, M., & Thaddeus, P. 1988, *ApJ*, 311, L95
- Combes, F., & Wiklind, T. 1995, *A&A*, 303, L61
- Comito, C., Schilke, P., Phillips, T. G., Lis, D. C., Motte, F., & Mehringer, D. 2005, *ApJS*, 156, 127
- Cox, P., Güsten, R., & Henkel, C. 1988, *A&A*, 206, 108
- Dickens, J. E., & Irvine, W. M. 1999, *ApJ*, 518, 733
- Flower, D. R. 2001, *J. Phys. B.: At. Mol. Opt. Phys.*, 34, 2731

- Fontani, F., Caselli, P., Crapsi, A. et al. 2006, *A&A*, 460, 709
- Frerking, M. A., Langer, W. D., & Wilson, R. W. 1982, *ApJ*, 262, 590
- Fuente, A., Martín-Pintado, J., & Gaume, R. 1995, *ApJ*, 442, L33
- Fuente, A., García-Burillo, S., Gerin, M., et al. 2006, *ApJ*, 641, L105
- Gerin, M., Roueff, E. 1999, in *Highly Redshifted Radio Lines*, ASP Conf. Ser. 156, eds. C. Carilli et al. San Francisco, p196
- Green, S. 1991, *ApJS*, 76, 979
- Green, S. 1994, *ApJ*, 434, 188
- Green, S., & Chapman, S. 1978, *ApJS*, 37, 169
- Güsten, R., Nyman, L. A., Schilke, P., Menten, K. M., Cesarsky, C., & Booth, R. 2006, *A&A* 454, L13
- Heikkilä, A., Johansson, L. E. B., & Olofsson, H. 1997, *A&A*, 319, L21
- Heikkilä, A., Johansson, L. E. B., & Olofsson, H. 1998, *A&A*, 332, 493
- Heikkilä, A., Johansson, L. E. B., & Olofsson, H. 1999, *A&A*, 344, 817
- Henkel, C., Mauersberger, R. 1993, *A&A* 274, 730
- Henkel, C., Jacq, T., Mauersberger, R., Menten, K. M., Steppe, H. 1987, *A&A*, 188, L1
- Hodge, P. 1989, *ARA&A*, 27, 139
- Hunter, I., et al. 2007, *A&A*, 466, 277
- Israel, F. P., Maloney, P. R., Geis, N., Herrmann, F., Madden, S. C., Poglitsch, A., & Stacey, G. J. 1996, *ApJ*, 465, 738
- Israel, F. P., et al. 2003, *A&A*, 406, 817
- Jansen, D. J., Spaans, M., Hogerheijde, M. R., & van Dishoeck, E. F. 1995, *A&A*, 303, 541
- Johansson, L. E. B., Olofsson, H., Hjalmarson, A., Gredel, R., & Black, J. H. 1994, *A&A*, 291, 89
- Kalenskii, S. V., Dzura, A. M., Booth, R. S., Winnberg, A., & Alakoz, A. V. 1997, *A&A*, 321, 311

- Kahane, C., Lucas, R., Frerking, M. A., Langer, W. D., & Encrenaz, P. 1984, *A&A*, 137, 211
- Klein, B., Philipp, S. D., Krämer, I., Kasemann, C., Güsten, R., Menten, K. M. 2006, *A&A* 454, L29
- Langer, W. D., Graedel, T. E., Frerking, M. A., & Armentrout, P. B. 1984, *ApJ*, 277, 581
- Larson, R. B. 1981, *MNRAS*, 194, 809
- Lazendic, J. S., Whiteoak, J. B., Klammer, I., Harbison, P. D., & Kuiper, T. B. H. 2002, *MNRAS*, 331, 969
- Leung, C. M., Herbst, E., Huebner, W. F. 1984, *ApJS*, 56, 231
- Liechti, S., & Walmsley, C. M. 1997, *A&A*, 321, 625
- Lovas, F. J., & Krupenie, P. H. 1974, *J. Phys. Chem. Ref. Data*, 3, 245
- MacLaren, I., Richardson, K. M., & Wolfendale, A. W. 1988, *ApJ*, 333, 821
- Madden, S. C., Irvine, W. M., Swade, D. A., Matthews, H. E., & Friberg, P. 1989, *AJ*, 97, 1403
- Mangum, J. G. & Wootten, A. 1993, *ApJS*, 89, 123
- Martín, S., Mauersberger, R., Martín-Pintado, J., Henkel, C., & García-Burillo, S. 2006, *ApJS*, 164, 450
- Mauersberger, R., Henkel, C., Wielebinski, R., Wiklind, T., & Reuter, H.-P. 1996a, *A&A*, 305, 421
- Mauersberger, R., Henkel, C., Whiteoak, J. B., Chin, Y.-N., & Tieftrunk, A. R. 1996b, *A&A*, 309, 705
- Mauersberger, R., Ott, U., Henkel, C., Cernicharo, J. & Gallino, R. 2004, *A&A* 426, 219
- Milam, S. N., Savage, C., Brewster, M. A., Ziurys, L. M., & Wyckoff, S. 2005, *ApJ*, 634, 1126
- Mizuno, N., Muller, E., Maeda, H., Kawamura, A., Minamidani, T., Onishisi, T., Mizuno, A., & Fukui, Y. 2006, *ApJ*, 634, L107
- Mühle, S., Seaquist, E. R., & Henkel, C. 2007, *ApJ*, 671, 1579

- Muller, S., Guélin, M., Dumke, M., Lucas, R., & Combes, F. 2006, *A&A*, 458, 417
- Oliveira, J. M., van Loon, J. Th., Stanimirović, S., & Zijlstra, A. A. 2006, *MNRAS*, 372, 1509
- Origlia, L., Ranalli, P., Comastri, A., & Maiolino, R. 2004, *ApJ*, 606, 862
- Parise, B., Ceccarelli, C., Tielens, A. G. G. M., Castets, A., Caux, E., Lefloch, B., & Maret, S. 2006, *A&A*, 453, 949
- Penzias, A. A. 1981, *ApJ*, 249, 518
- Pety, J., Teyssier, D., Fossé, D., Roueff, E., Abergel, A., Habart, E., & Cernicharo, J. 2005, *A&A*, 435, 885
- Pratap, P., Dickens, J. E., Snell, R. L., Miralles, M. P., Bergin, E. A., Irwin, W. M., & Schloerb, F. P. 1997, *ApJ*, 486, 862
- Risacher, C. et al. 2006, *A&A*, 454, L17
- Roberts, H., Fuller, G.A., Millar, T. J., Hatchell, J., & Buckle, J. V. 2002, *A&A*, 381, 1026
- Rubio, M., Garay, G., Montani, J., & Thaddeus, P. 1991, *ApJ*, 368, 173
- Rubio, M., Lequeux, J., & Boulanger, F. 1993, *A&A*, 271, 9
- Schilke, P., Walmsley, C. M., Pineau de Forêts, G., Roueff, E., Flower, D. R., & Guilloteau, S. 1992, *A&A*, 256, 595
- Schöier, F. L., van der Tak, F. F. S., van Dishoeck, E. F., & Black, J. H. 2005, *A&A*, 432, 369
- Scoville, N. Z., & Solomon, P. M. 1974, *ApJ*, 187, L67
- Skatrud, D. D., De Lucia, F. C., Blake, G. A., & Sastry, K. V. L. N. 1983, *J. Mol. Spec.*, 99, 35
- Sobolev, V. V. 1960, in *Moving Envelopes of Stars* (Cambridge, Harvard University Press)
- Thaddeus, P., Vrtilek, J. M., & Gottlieb, C. A. 1985, *ApJ*, 299, 63
- Turner, B. E., Chan, K.-W., Green, S., & Lubowich, D. A. 1992, *ApJ*, 399, 114
- van der Tak, F. F. S., Black, J. H., Schöier, F. L., Jansen, D. J., & van Dishoeck, E. F. 2007, *A&A*, 468, 627

- Wang, M., Henkel, C., Chin, Y.-N., Whiteoak, J. B., Hunt Cunningham, M., Mauersberger, R., & Muders, D. 2004, *A&A*, 422, 883
- Watson, W. D., Anicich, V. G., & Huntress, W. T. 1976, *ApJ*, 205, L165
- Wei, A., Neininger, N., Henkel, C., Stutzki, J., & Klein, U. 2001, *A&A*, 554, 143
- Westerlund, B. E. 1990, *A&AR*, 2, 29
- Wheeler, J. C., Sneden, C., & Truran, J. W. 1989, *ARA&A*, 27, 279
- Whiteoak, J. B., & Gardner, F. F. 1986, *MNRAS*, 222, 513
- Wilcots, E. M. 1994, *AJ*, 108, 1674
- Wilson, T. L., & Rood, R. 1994, *ARA&A*, 32, 191
- Wong, T., Whiteoak, J. B., Ott, J., Chin, Y.-N., & Cunningham, M. R. 2006, *ApJ*, 649, 224
- Wouterloot, J. G. A., & Brand, J. 1996, *A&AS*, 119, 439
- Wouterloot, J. G. A., & Walmsley, C. M. 1986, *A&A*, 168, 237
- Wouterloot, J. G. A., Brand, J., & Henkel, C. 2005, *A&A*, 430, 549
- Wouterloot, J. G. A., Henkel, C., Brand, J., & Davis, G. R. 2008, *A&A*, 487, 237
- Yamaguchi, R., Mizuno, N., Onishi, T. Mizuno, A., & Fukui, Y. 2001, *PASJ*, 53, 985

Table 1. Spectroscopic parameters

ν (GHz)	Telescope	$\theta_b^{\text{a)}$ ($''$)	$\theta_b^{\text{a)}$ (pc)	$T_{\text{sys}}^{\text{b)}$ (K)	$\eta_b^{\text{c)}$
85–98	SEST	61–53	15–13	180–270	0.77–0.74
109–219	SEST	47–24	11–5.8	250–400	0.70–0.48
220–245	SEST	23–21	5.6–5.1	550–1000	0.48–0.44
265–268	SEST	20–19	4.8–4.6	~ 2000	0.41–0.40
330–357	SEST	16–14	3.9–3.4	~ 3000	0.32–0.30
345	APEX	20	4.8	~ 500	0.73

^{a)}Full Width to Half Power (FWHP) beam widths. To establish linear scales, $D=50$ kpc was adopted.

^{b)}Single sideband system temperatures in units of main beam brightness temperature (T_{mb})

^{c)}SEST beam efficiencies were derived from measurements of Jupiter (L. Knee, priv. comm.). For the beam and forward hemisphere efficiency of APEX, see Güsten et al. (2006).

Table 2. Line parameters

Transition	Frequency (MHz)	Detection ^{a)}	$\int T_{\text{mb}} dv^{\text{b)}$ (K km s ⁻¹)	$v_{\text{LSR}}^{\text{c)}$ (km s ⁻¹)	$\Delta v_{1/2}^{\text{c)}$ (km s ⁻¹)	rms ^{d)} (K)	Dv ^{e)} (km s ⁻¹)
c-C ₃ H ₂ 2 _{1,2} -1 _{0,1}	85338.890	+	0.20±0.04	235.92±0.18	2.83±0.86	0.01	0.86
HC ¹⁵ N 1-0	86054.961	?	0.03±0.01	234.76±0.27	3.96±1.05	0.01	0.87
H ¹³ CN 1-0	86340.184	+	0.08±0.01	236.76±0.52	7.41±0.90	0.01	0.87
H ¹³ CO ⁺ 1-0	86754.294	+	0.09±0.01	234.94±0.17	3.35±0.46	0.01	0.89
C ₂ H 1-0 $J=3/2-1/2$ $F=2-1$	87316.925	+	0.87±0.05	236.23±0.15	5.41±0.39	0.04	0.89
C ₂ H 1-0 $J=3/2-1/2$ $F=1-0$	87328.624	+	0.36±0.05	235.71±0.35	4.76±0.74	0.04	0.89
HCN 1-0 $F=1-1$	88630.416		0.81±0.01	235.04±0.04	4.80±0.04	0.01	0.85
HCN 1-0 $F=2-1$	88631.847	+	1.26±0.01	235.04±0.04	4.80±0.04	0.01	0.85
HCN 1-0 $F=0-1$	88633.936		0.35±0.01	235.05±0.04	4.80±0.04	0.01	0.85
HCO ⁺ 1-0	89188.518	+	3.56±0.09	235.12±0.07	5.67±0.18	0.07	0.87
HNC 1-0	90663.543	+	0.94±0.04	235.23±0.11	5.14±0.23	0.02	0.99
HC ₃ N 10-9	90978.993	?	0.12±0.02	237.53±0.75	9.52±1.38	0.01	0.96
¹³ CS 2-1	92494.299	+	0.06±0.02	238.33±1.32	4.77±2.25	0.01	0.98
N ₂ H ⁺ 1-0	93173.404	+	0.36±0.03	237.09±0.33	8.80±0.69	0.02	0.97
C ³⁴ S 2-1	96412.982	+	0.15±0.01	235.21±0.19	4.39±0.53	0.01	0.94
CH ₃ OH 2 ₋₁ -1 ₋₁ E	96739.390	+	0.10±0.02	235.90±0.31	3.58±0.67	0.02	0.93
CH ₃ OH 2 ₀ -1 ₀ A+	96741.420	+	0.16±0.02	235.05±0.20	3.76±0.44	0.02	0.93
CS 2-1	97980.968	+	2.02±0.06	235.24±0.07	5.08±0.17	0.05	0.89
C ¹⁸ O 1-0	109782.160	+	0.15±0.01	235.30±0.14	3.27±0.35	0.01	0.94
¹³ CO 1-0	110201.353	+	5.97±0.10	235.41±0.04	4.50±0.09	0.09	0.94
C ¹⁷ O 1-0	112358.988	+	0.09±0.01	235.01±0.42	7.25±0.75	0.01	0.92
CN 1-0, $J=1/2-1/2$ $F=1/2-1/2$	113144.122	+	0.27±0.03	234.83±0.30	5.47±0.74	0.02	0.91
CN 1-0, $J=1/2-1/2$ $F=3/2-1/2$	113170.502	+	0.38±0.03	235.10±0.17	5.03±0.43	0.02	0.91
CN 1-0, $J=1/2-1/2$ $F=3/2-3/2$	113191.287	+	0.40±0.03	235.39±0.17	5.21±0.41	0.02	0.91
CN 1-0, $J=3/2-1/2$ $F=3/2-1/2$	113488.140	+	0.35±0.02	235.19±0.05	4.61±0.40	0.02	0.91
CN 1-0, $J=3/2-1/2$ $F=5/2-3/2$	113490.982	+	0.80±0.02	235.25±0.05	4.54±0.18	0.02	0.91
CN 1-0, $J=3/2-1/2$ $F=1/2-1/2$	113499.639	+	0.33±0.02	235.18±0.05	5.88±0.52	0.02	0.91
CN 1-0, $J=3/2-1/2$ $F=3/2-3/2$	113508.944	+	0.32±0.02	235.26±0.05	4.44±0.35	0.02	0.91
CO 1-0	115271.204	+	49.21±0.31	235.25±0.02	5.79±0.04	0.25	0.90
HDCO 2 _{0,2} -1 _{0,1}	128812.860	–	0.02	0.88
HDCO 2 _{1,1} -1 _{1,0}	134284.910	–	0.01	0.93
SO ₂ 5 _{1,5} -4 _{0,4}	135696.011	+	4.28±0.01	235.04±0.17	3.15±0.30	0.01	0.92
SO 4 ₃ -3 ₂	138178.648	+	1.15±0.04	235.01±0.07	4.56±0.18	0.04	0.93
¹³ CS 3-2	138739.309	+	0.07±0.01	234.54±0.23	4.00±0.56	0.01	0.93
DCO ⁺ 2-1	144077.321	+	0.17±0.01	235.37±0.20	5.17±0.42	0.01	0.89
H ₂ CO 2 _{1,2} -1 _{1,1}	140839.518	+	1.84±0.05	235.14±0.07	5.35±0.19	0.05	0.92
C ³⁴ S 3-2	144617.147	+	0.23±0.02	234.82±0.11	3.29±0.27	0.02	0.89
DCN 2-1	144828.000	?	0.06±0.02	234.45±1.14	7.07±1.49	0.01	0.89
CH ₃ OH 3 ₋₁ -2 ₋₁ E	145097.470	+	0.31±0.02	234.92±0.12	4.23±0.44	0.02	0.89
CH ₃ OH 3 ₀ -2 ₀ A+	145103.230	+	0.39±0.02	234.92±0.12	5.44±0.35	0.02	0.89
HC ₃ N 16-15	145560.946	?	0.09±0.02	235.82±0.43	3.71±0.88	0.01	0.89
H ₂ CO 2 _{0,2} -1 _{0,1}	145602.953	+	1.18±0.04	235.35±0.09	5.40±0.21	0.04	0.89
C ³³ S 3-2	145755.620	?	0.06±0.01	238.38±0.53	4.65±1.20	0.01	0.86
CS 3-2	146969.049	+	2.61±0.11	235.13±0.09	4.60±0.21	0.11	0.88
NO 2Π _{1/2} $J=3/2-1/2$ $F=5/2-1/2$	150176.480	–	0.01	0.86

Table 2—Continued

Transition	Frequency (MHz)	Detection ^{a)}	$\int T_{\text{mb}} dv^{\text{b)}}$ (K km s ⁻¹)	$v_{\text{LSR}}^{\text{c)}}$ (km s ⁻¹)	$\Delta v_{1/2}^{\text{c)}}$ (km s ⁻¹)	rms ^{d)} (K)	Dv ^{e)} (km s ⁻¹)
H ₂ CO 2 _{1,1} –1 _{1,0}	150498.339	+	1.68±0.05	235.45±0.08	5.44±0.19	0.05	0.86
c-C ₃ H ₂ 4 _{1,4} –3 _{0,3}	150851.910	+	0.15±0.01	235.25±0.19	3.63±0.32	0.01	0.86
HNCO 7 _{0,7} –6 _{0,6}	153865.092	–	0.02	0.84
H ₂ CO 3 _{0,3} –2 _{0,2}	218222.188	+	0.62±0.05	233.24±0.19	4.68±0.41	0.02	0.96
H ₂ CO 3 _{2,2} –2 _{2,1}	218475.641	–	0.03	0.92
H ₂ CO 3 _{2,1} –2 _{2,0}	218760.068	–	0.03	0.96
¹³ CO 2–1	220398.686	+	13.64±0.07	235.01±0.01	4.46±0.03	0.09	0.91
H ₂ CO 3 _{1,2} –2 _{1,1}	225697.772	+	1.24±0.07	235.16±0.15	6.35±0.47	0.07	0.96
CN 2–1, $J=3/2-1/2$ $F=5/2-3/2$	226659.543	+	0.37±0.05	234.39±0.24	4.09±0.63	0.06	0.96
CN 2–1, $J=3/2-1/2$ $F=3/2-1/2$	226679.341	+	0.26±0.04	235.18±0.38	4.39±0.80	0.06	0.96
CN 2–1, $J=5/2-3/2$ $F=7/2-5/2$	226874.764	+	1.10±0.05	234.52±0.13	5.75±0.37	0.06	0.96
CO 2–1	230537.990	+	78.19±0.20	235.05±0.01	5.77±0.02	0.24	0.87
C ³⁴ S 5–4	241016.176	?	0.18±0.04	232.30±0.47	4.20±0.76	0.02	0.93
CS 5–4	244935.606	+	1.77±0.05	234.48±0.06	4.38±0.17	0.07	0.92
HCN 3–2	265886.432	+	1.24±0.09	234.51±0.29	8.06±0.66	0.09	0.79
HCO ⁺ 3–2	267557.625	+	2.67±0.25	235.17±0.32	8.04±1.06	0.23	0.94
¹³ CO 3–2	330587.957	+	17.73±0.65	234.80±0.08	4.78±0.23	0.94	0.91
CS 7–6	342882.949	?	0.85±0.13	234.36±0.24	3.74±0.77	0.08	0.88
CO 3–2	345795.975	+	79.76±0.53	235.10±0.02	6.16±0.05	0.75	0.87
HCO ⁺ 4–3	356734.490	+	2.60±0.22	233.93±0.22	5.47±0.55	0.32	0.88

^{a)}‘+’: detection; ‘–’: non-detection; ‘?’: tentative detection.

^{b)}Integrated from 220 to 240 km s⁻¹ after subtracting a first order baseline or a constant offset in T_{A}^* . The errors were derived from Gaussian fits and do not account for calibration and pointing uncertainties.

^{c)}Obtained from single component Gaussian fits. $v_{\text{LSR}} = v_{\text{HEL}} - 4.5 \text{ km s}^{-1}$

^{d)}rms values for a $\sim 1 \text{ km s}^{-1}$ channel width on a T_{mb} scale.

^{e)}Channel spacings after smoothing as shown in Figs. 3–6.

Table 3. Half power source sizes of the 1.2 mm continuum and the mm-wave line emission (see Sect. 3) observed with the SEST

Transition		θ_b ^{a)}	$\Delta\alpha$ ^{b)}	$\Delta\delta$ ^{c)}	$\theta_{s,\alpha}$ ^{d)}	$\theta_{s,\delta}$ ^{d)}	θ_s ^{d)}
		(")					
250 GHz	Cont.	24	46	46	39	39	39
(1.2 mm)							
CO	1–0	45	80	70	66	54	60
	2–1	23	60	60	56	56	56
	3–2	15	45	40	42	37	40
¹³ CO	1–0	47	65	60	45	37	41
	2–1	24	40	35	32	26	29
CS	3–2	35	42	50	23	35	30
	5–4	21	40	53	34	49	42
HCO ⁺	1–0	58	60	60	15	15	15
HCN	1–0	58	60	54	13	—	—
H ₂ CO	2–1	37	45	54	26	39	33

^{a)} θ_b , full width to half power (FWHP) beam width at the transition observed

^{b)} $\Delta\alpha$, measured full half width in Right Ascension

^{c)} $\Delta\delta$, measured full half width in Declination

^{d)} $\Delta\alpha^2 - \theta_b^2 = \theta_{s,\alpha}^2$; $\Delta\delta^2 - \theta_b^2 = \theta_{s,\delta}^2$; $\theta_s^2 = (\theta_{s,\alpha}^2 + \theta_{s,\delta}^2)/2$

Table 4. Line intensities

Transition	T_{mb} (K)	θ_s (")	η_{bf}	T'_{mb} (K)
CO 1–0	8.853	60	0.640	13.833
CO 2–1	10.662	56	0.861	12.385
CO 3–2	12.171	40	0.877	13.884
^{13}CO 1–0	1.248	40	0.419	2.978
^{13}CO 2–1	2.244	40	0.743	3.021
^{13}CO 3–2	3.487	40	0.867	4.024
C^{18}O 1–0	0.044	40	0.417	0.105
C^{17}O 1–0	0.011	40	0.429	0.026
CS 2–1	0.415	40	0.363	1.141
CS 3–2	0.547	40	0.562	0.972
CS 5–4	0.281	40	0.781	0.359
CS 7–6	0.215	40	0.875	0.245
C^{34}S 2–1	0.032	40	0.356	0.091
C^{34}S 3–2	0.064	40	0.554	0.116
C^{34}S 5–4	0.041	40	0.775	0.053
C^{33}S 3–2	0.012	40	0.558	0.022
^{13}CS 2–1	0.012	40	0.337	0.037
^{13}CS 3–2	0.016	40	0.533	0.030
C_3H_2 2 _{1,2} –1 _{0,1}	0.058	40	0.302	0.193
C_3H_2 4 _{1,4} –3 _{0,3}	0.040	40	0.575	0.069
H_2CO 2 _{1,2} –1 _{1,1}	0.333	40	0.541	0.616
H_2CO 2 _{0,2} –1 _{0,1}	0.205	40	0.558	0.369
H_2CO 2 _{1,1} –1 _{1,0}	0.289	40	0.574	0.504
H_2CO 3 _{0,3} –2 _{0,2}	0.143	40	0.739	0.194
H_2CO 3 _{1,2} –2 _{1,1}	0.183	40	0.752	0.244
N_2H^+ 1–0	0.039	40	0.340	0.114
C_2H 1–0 3/2–1/2 F=2–1	0.152	40	0.312	0.486
C_2H 1–0 3/2–1/2 F=1–0	0.070	40	0.312	0.226
HNC 1–0	0.172	40	0.328	0.525
HCN 1–0	0.158	40	0.319	0.495
HCN 1–0	0.260	40	0.319	0.815
HCN 1–0	0.068	40	0.319	0.213
HCN 3–2	0.160	40	0.815	0.196
H^{13}CN 1–0	0.009	40	0.307	0.029
HC^{15}N 1–0	0.007	40	0.305	0.022
DCN 2–1	0.010	40	0.555	0.018
DCO^+ 2–1	0.029	40	0.553	0.052
H^{13}CO^+ 1–0	0.022	40	0.310	0.071
HCO^+ 1–0	0.590	40	0.322	1.832
HCO^+ 3–2	0.419	40	0.829	0.505
HCO^+ 4–3	0.325	40	0.883	0.368
HC_3N 10–9	0.012	40	0.330	0.035

Table 4—Continued

Transition	T_{mb} (K)	θ_{s} (")	η_{bf}	T'_{mb} (K)
HC ₃ N 16–15	0.012	40	0.558	0.022
SO ₂ 5 _{1,5} -4 _{0,4}	0.013	40	0.523	0.025
SO 4 ₃ -3 ₂	0.236	40	0.532	0.445
CH ₃ OH 2 ₀ -1 ₀ A ⁺	0.041	40	0.357	0.115
CH ₃ OH 2 ₀ -1 ₀ E ⁺	0.026	40	0.357	0.073
CH ₃ OH 3 ₀ -2 ₀ A ⁺	0.068	40	0.556	0.122
CH ₃ OH 3 ₀ -2 ₀ E ⁺	0.069	40	0.556	0.124
CN 1-0 3/2-1/2 F=3/2-1/2	0.071	40	0.434	0.165
CN 1-0 3/2-1/2 F=5/2-3/2	0.166	40	0.434	0.382
CN 1-0 3/2-1/2 F=1/2-1/2	0.053	40	0.434	0.122
CN 1-0 3/2-1/2 F=3/2-3/2	0.068	40	0.434	0.157
CN 1-0 1/2-1/2 F=1/2-3/2	0.046	40	0.432	0.108
CN 1-0 1/2-1/2 F=3/2-1/2	0.071	40	0.432	0.165
CN 1-0 1/2-1/2 F=3/2-3/2	0.072	40	0.432	0.166
CN 2-1 3/2-1/2 F=5/2-3/2	0.085	40	0.753	0.113
CN 2-1 3/2-1/2 F=3/2-1/2	0.056	40	0.753	0.075
CN 2-1 5/2-3/2 F=7/2-5/2	0.179	40	0.754	0.237

Table 5. Source averaged logarithmic column densities and densities

Molecule	Column density (cm ⁻²)	$n(\text{H}_2)$ for $T_{\text{kin}}^{\text{a)}$		
		20 K	50 K	100 K
		(cm ⁻³)		
CO	17.8	3.7	3.7	3.7
CN	13.5	—	—	—
CS	13.4	6.0	5.7	5.3
SO ^{a)}	13.2	—	—	—
SO ₂ ^{a)}	12.7	—	—	—
HCN	12.8	6.0	5.6	5.3
HCO ⁺	12.6	5.8	5.6	5.3
HNC	12.4	—	—	—
N ₂ H ⁺ ^{a)}	11.8	—	—	—
Para-H ₂ CO	12.6	6.0	5.7	5.3
Ortho-H ₂ CO	13.1	6.0	5.7	5.4
c-C ₃ H ₂	12.5	5.0	4.7	4.5
HC ₃ N ^{b)}	11.8	—	5.5	5.2
CH ₃ OH	13.0	5.4	4.5	4.3

^{a)}Median for densities of 5×10^4 and $5 \times 10^5 \text{ cm}^{-3}$ and $T_{\text{kin}} = 50 \text{ K}$. See Sect. 4.3.2.

^{b)}Based on two tentative detections. The given column density is thus a firm upper limit.

Table 6. Source averaged logarithmic column densities relative to CO toward N 113 and selected galactic targets^{a)}.

Molecule	Column density (cm ⁻²)				
	N 113	Orion			TMC-1
		Hot Core	Ridge	Bar	
CN	–4.3	—	–4.2	–4.2	–5.4
CS	–4.4	–4.3	–4.3	–3.6	–4.8
SO	–4.6	–3.3	≲–4.7	–4.0	–5.1
SO ₂	–5.1	–3.1	<–4.2	–5.9	—
HCN	–5.0	–2.9	–4.0	–4.3	–4.2
HCO ⁺	–5.2	–5.3	–4.3	–4.5	–4.3
HNC	–5.4	–5.1	–5.0	–5.0	–3.8
N ₂ H ⁺	–6.0	—	—	—	–5.8
H ₂ CO	–4.6	–4.5	—	–4.2	–3.7
c-C ₃ H ₂	–5.3	—	—	—	–4.0
HC ₃ N	≲–6.0	–4.9	–5.6	—	–4.6
CH ₃ OH	–4.8	–3.2	—	–5.0	–4.7

^{a)}Data for the Orion Hot Core and Ridge were taken from Blake et al. (1987) and Comito et al. (2005). Abundances for the Orion Bar refer to the (20'', –20'') position of Jansen et al. (1995). TMC-1 values were adopted from Leung et al. (1984), Madden et al. (1989), and Pratap et al. (1997) for the cyanopolyne peak.

Table 7. Source averaged logarithmic column densities relative to CO toward N 113 and other selected extragalactic targets^{a)}.

Molecule	Column density (cm ⁻²)				
	N 113	N 159W	M 82	NGC 253	NGC 4945
CN	−4.3	−4.2	−4.3	−4.5	−4.3
CS	−4.4	−4.3	−3.8	−4.6	−4.1
SO	−4.6	−4.3	<−4.4	−4.8	−4.7
SO ₂	−5.1	<−4.9	—	—	—
HCN	−5.0	−4.6	−3.9	−3.9	−3.5
HCO ⁺	−5.2	−4.7	−4.2	−3.6	≳−5.4
HNC	−5.4	−5.1	−4.6	−4.2	−3.4
N ₂ H ⁺	−6.0	—	−5.7	−5.8	−6.0
H ₂ CO	−4.6	−4.4	−3.4	−3.8	−4.5
c-C ₃ H ₂	−5.3	−4.6	−4.6	−5.1	−4.1
HC ₃ N	≲−6.0	<−5.2	−3.9	−3.8	−4.8
CH ₃ OH	−4.8	−4.4	<−4.6	−3.8	−3.9

^{a)} Assumed fractional CO abundance for N 159W: 1.2×10^{-5} ; for M 82, NGC 253, NGC 4945: 8×10^{-5} . Data were taken from Heikkilä et al. (1999), Wang et al. (2004) and Martín et al. (2006).

Table 8. Isotope Ratios

Isotope ratio	Solar system	Solar circle	Outer Galaxy	LMC (N113)	Proc. ^{a)}	Ref. ^(b)
$^{12}\text{C}/^{13}\text{C}$	89	70	100	49 ± 5	1	1,2
$^{14}\text{N}/^{15}\text{N}$	270	400	–	91 ± 21	2	1,3
$^{16}\text{O}/^{18}\text{O}$	490	560	–	2000 ± 250	3	1
$^{18}\text{O}/^{17}\text{O}$	5.5	4.1	5	1.7 ± 0.2	1	4
$^{32}\text{S}/^{34}\text{S}$	22	28	–	~ 15	4	5
$^{34}\text{S}/^{33}\text{S}$	6	6	–	≥ 6	4	5

^{a)}Primary processes of nucleosynthesis: (1) Helium burning/CNO burning; (2) CNO burning; (3) Helium burning; (4) Oxygen burning

^{b)}References: (1) Wilson & Rood (1994); (2) Wouterloot & Brand (1996); (3) Chin et al. (1999); (4) Wouterloot et al. (2005, 2008); (5) Chin et al. (1996a)

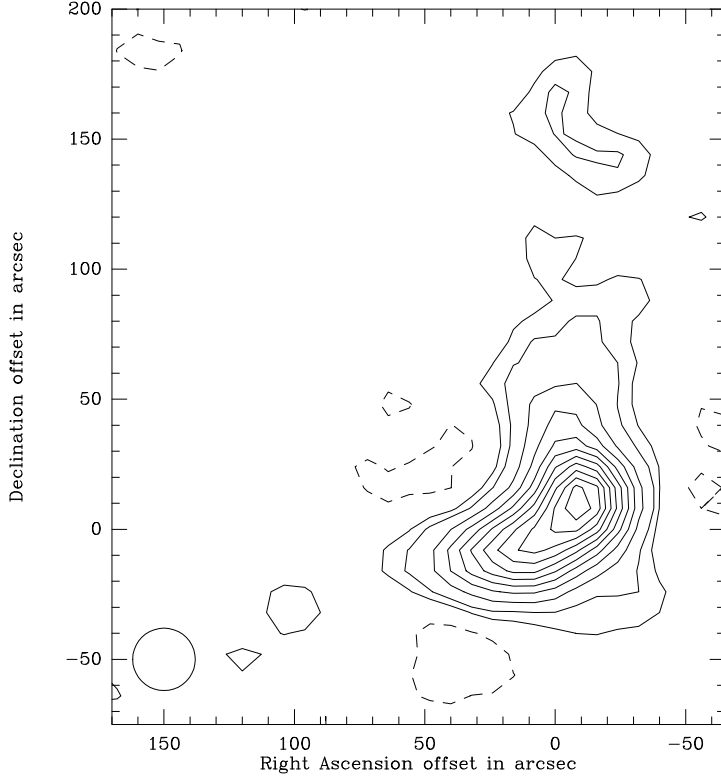


Fig. 1.— A $\lambda 1.2$ mm continuum map of N113. Contour levels are $-1, 1, 2, 4, 6, 8, \dots, 20$ times 19 mJy beam^{-1} ; the 1σ noise level is 7 mJy beam^{-1} . The peak is at $420 \text{ mJy beam}^{-1}$. The reference position is $\alpha_{\text{J2000}} = 05^{\text{h}} 13^{\text{m}} 18^{\text{s}}.2$, $\delta_{\text{J2000}} = -69^{\circ} 22' 35''$ ($\alpha_{\text{B1950}} = 05^{\text{h}} 13^{\text{m}} 38^{\text{s}}.7$, $\delta_{\text{B1950}} = -69^{\circ} 25' 57''$). The calibration is estimated to be accurate to $\pm 20\%$. Pointing uncertainty and beam size (the circle in the lower left corner) are $\pm 7''$ and $24''$, respectively.

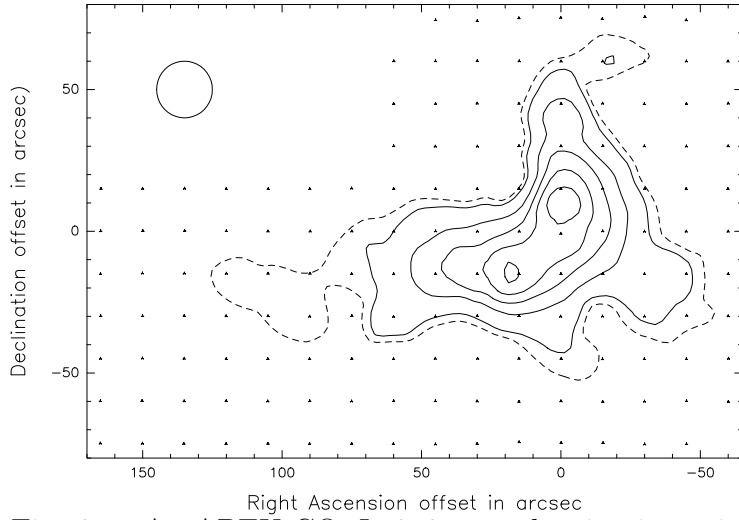


Fig. 2.— An APEX CO $J=3-2$ map showing intensities integrated over the Local Standard of Rest (LSR) velocity interval $225-245 \text{ km s}^{-1}$. Contours are 7 (dashed), 10, 20, 30, 40, and 50 K km s^{-1} on a T_{A}^* scale. The reference position is $\alpha_{\text{J2000}} = 05^{\text{h}} 13^{\text{m}} 18.^{\text{s}}.2$, $\delta_{\text{J2000}} = -69^{\circ} 22' 35''$. To convert to scales of main beam brightness temperature, multiply by 1.35. The calibration is estimated to be accurate to $\pm 15\%$. Pointing uncertainty and beam size (the circle in the upper left corner) are $\pm 3''$ and $20''$, respectively.

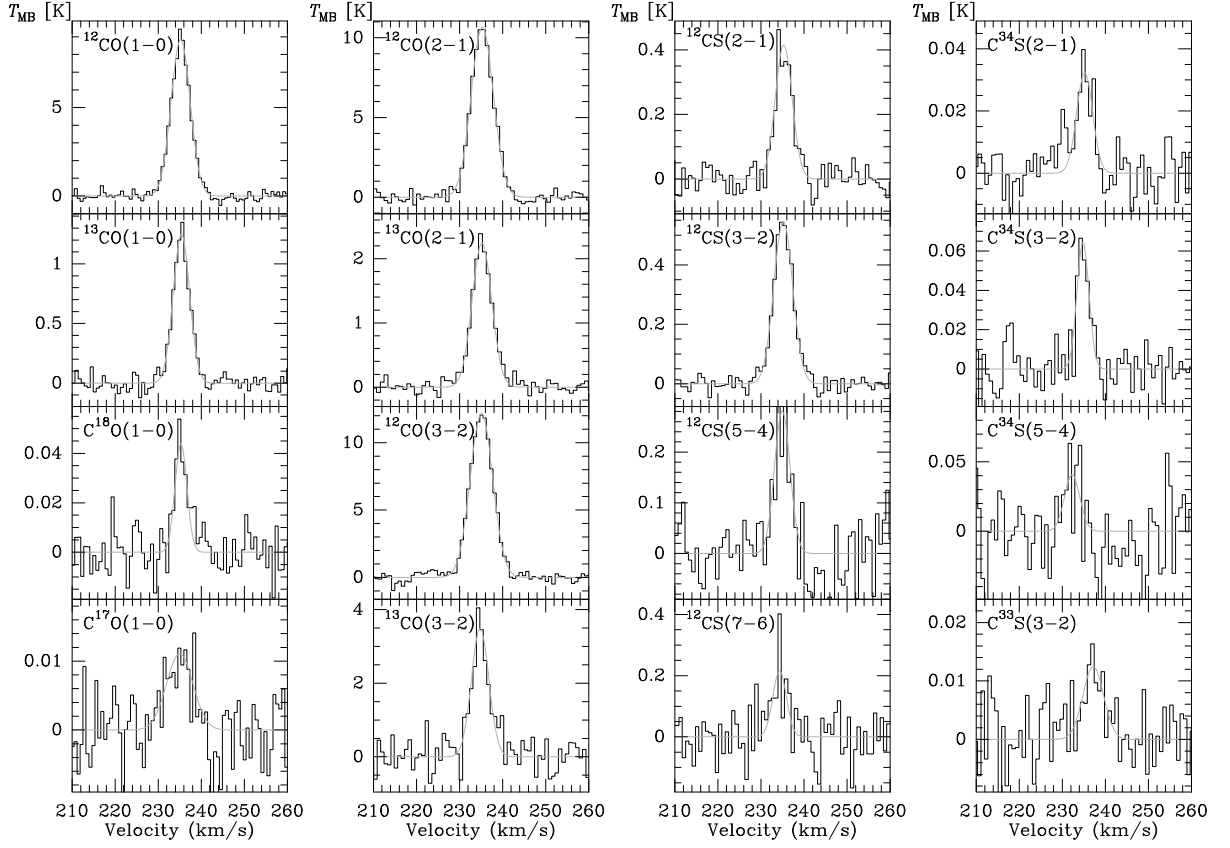


Fig. 3.— CO and CS spectra measured toward N113 ($\alpha = 05^{\text{h}}13^{\text{m}}18.2^{\text{s}}$, $\delta = -69^{\circ}22'35''$ (J2000)). The channel spacing for each spectrum is $\sim 0.9 \text{ km s}^{-1}$. Gaussian fits were performed for detected and tentatively detected lines, and resulting parameters are listed in Table 2 (same in Figs. 4–6).

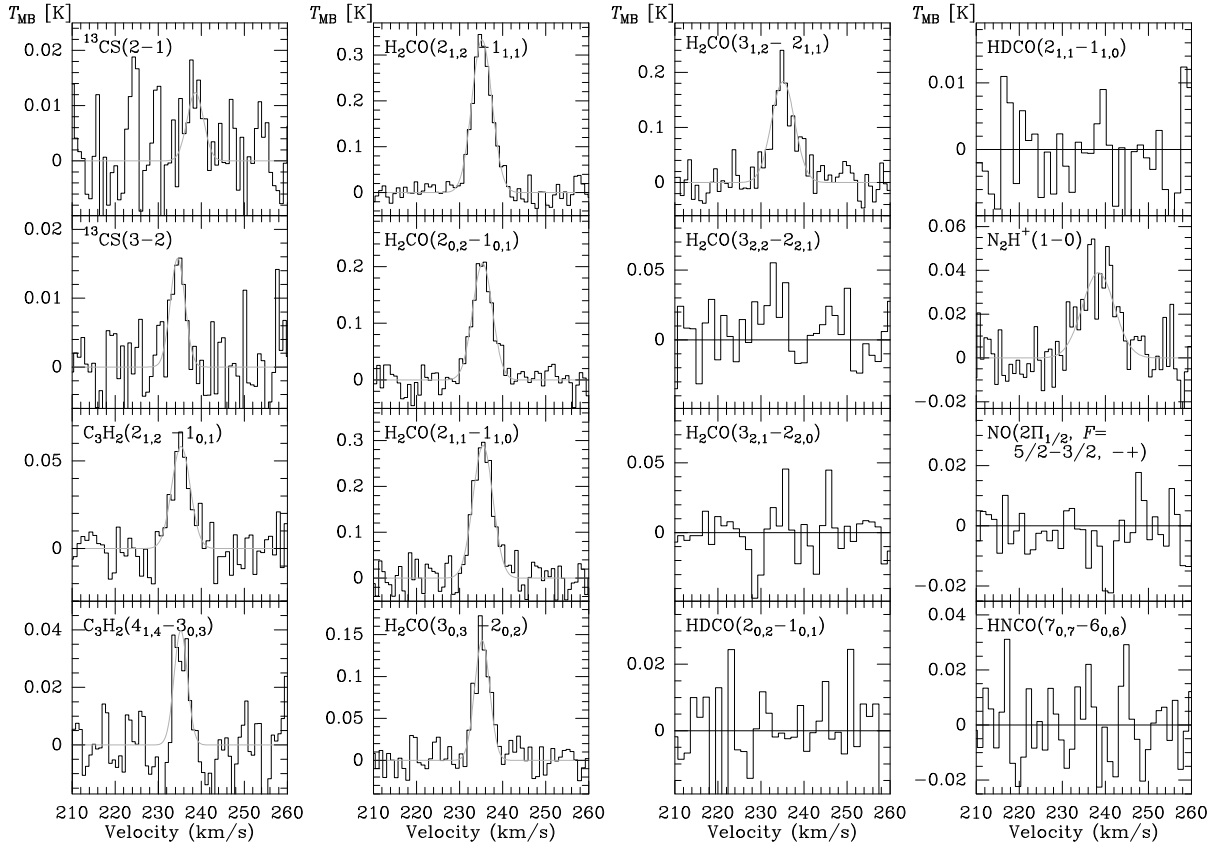


Fig. 4.— CS, C_3H_2 , H_2CO , HDCO, N_2H^+ , NO and HNCO spectra measured toward N113. In the case of N_2H^+ , the frequency of the main hyperfine component (93.713809 GHz) is taken as reference. In Table 2, however, the expected average frequency for optically thin emission and Local Thermodynamical Equilibrium is displayed. For further details, see Fig. 3.

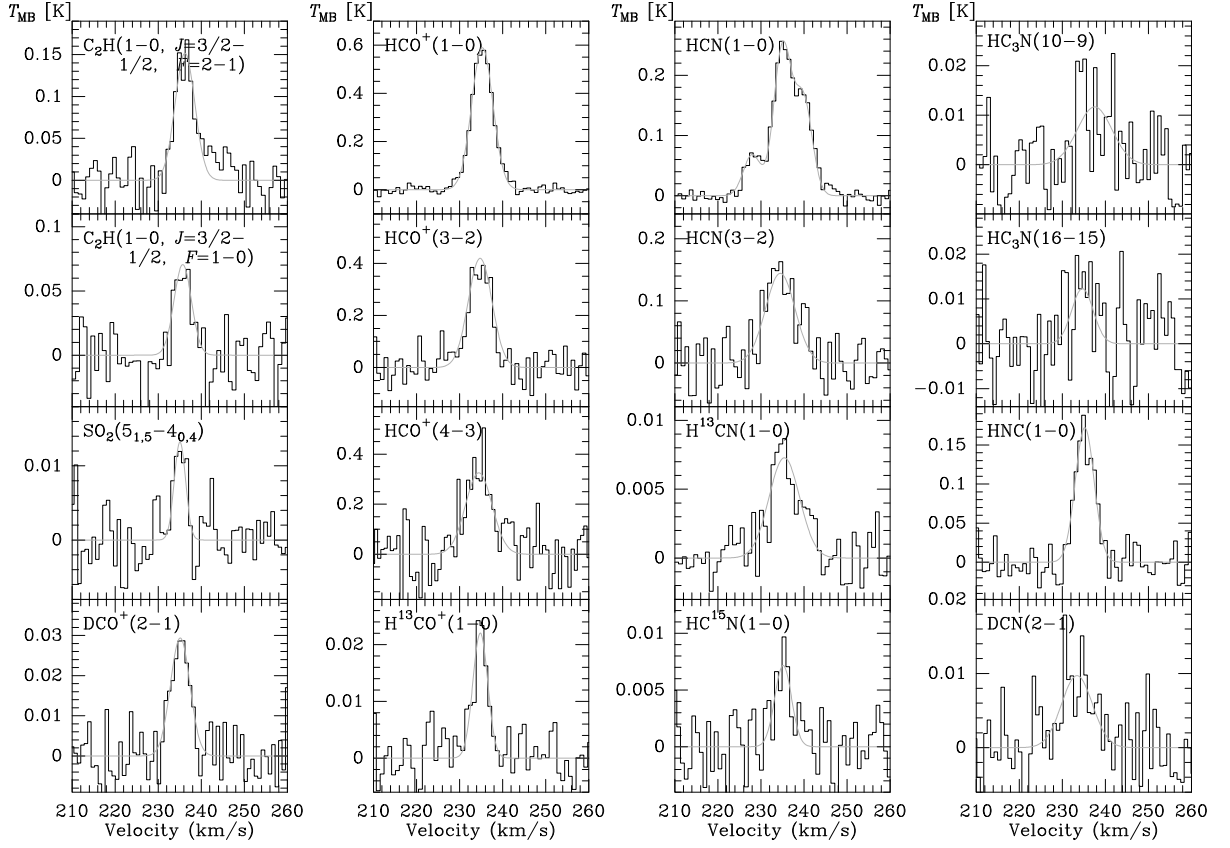


Fig. 5.— C_2H , SO_2 , DCO^+ , HCO^+ , HCN , HC_3N , HNC , and DCN spectra measured toward N113. For details, see Fig. 3.

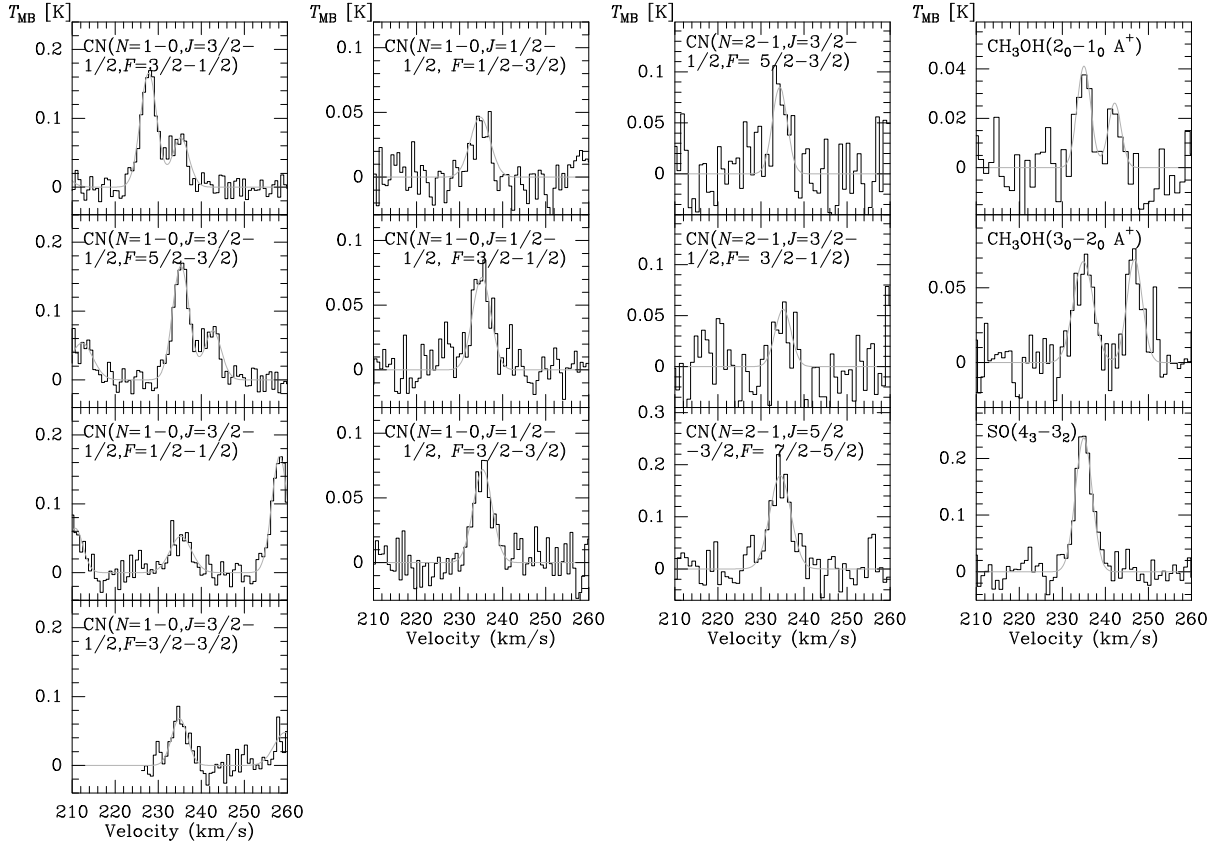


Fig. 6.— CN, CH₃OH, and SO spectra measured toward N113. The CH₃OH figures also show the $2_{-1}-1_{-1}$ E and $3_{-1}-2_{-1}$ E lines at slightly higher velocities than the 2_0-1_0 A⁺ and 3_0-2_0 A⁺ profiles, respectively. For further details, see Fig. 3.

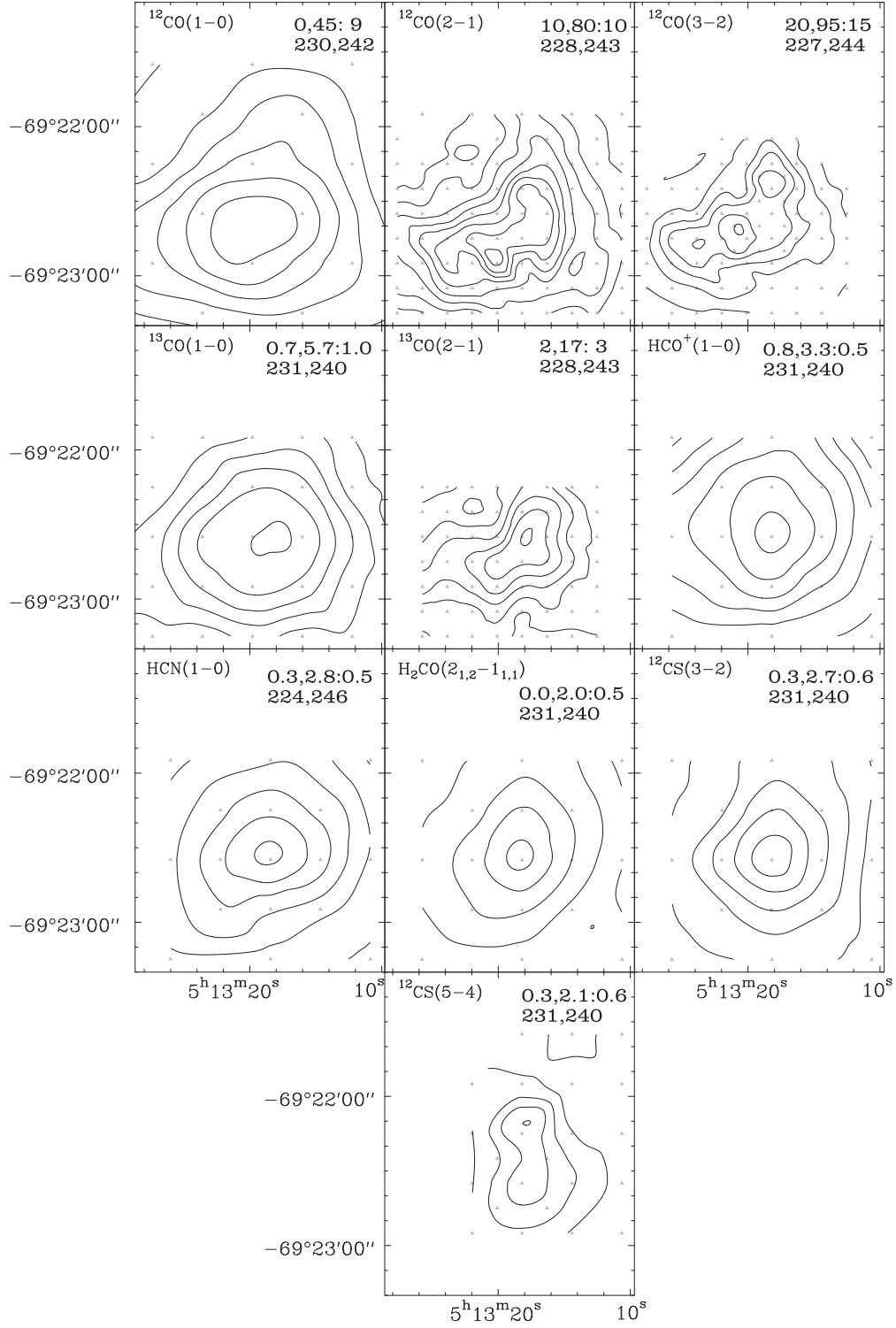


Fig. 7.— SEST CO, HCO⁺, HCN, H₂CO, and CS maps toward N113. The upper left corner of each panel indicates the molecular transition; the upper right corner gives the lowest contour, the highest contour, and the increment in K km s⁻¹ (upper line) and the velocity range in km s⁻¹ (lower line).

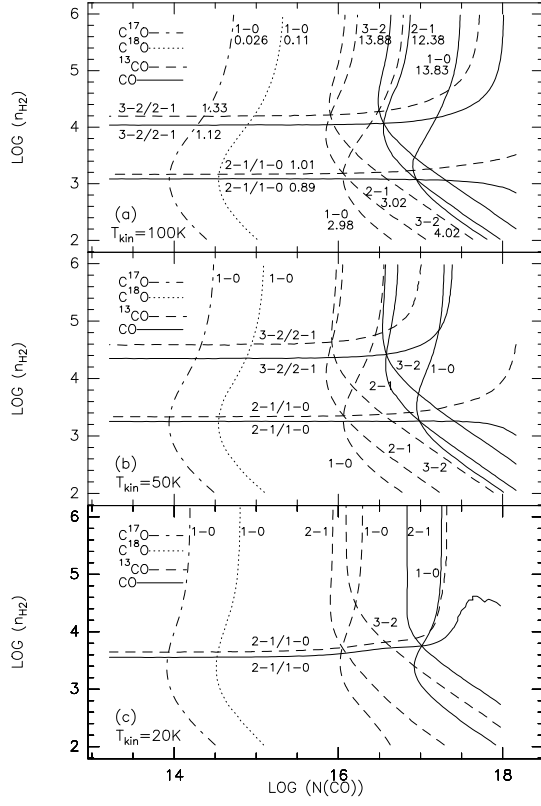


Fig. 8.— LVG calculations for C^{17}O (dash-dotted lines), C^{18}O (dotted lines), ^{13}CO (dashed lines) and CO (solid lines) at $T_{\text{kin}} \sim 100 \text{ K}$ (a), $T_{\text{kin}} \sim 50 \text{ K}$ (b) and $T_{\text{kin}} \sim 20 \text{ K}$ (c).

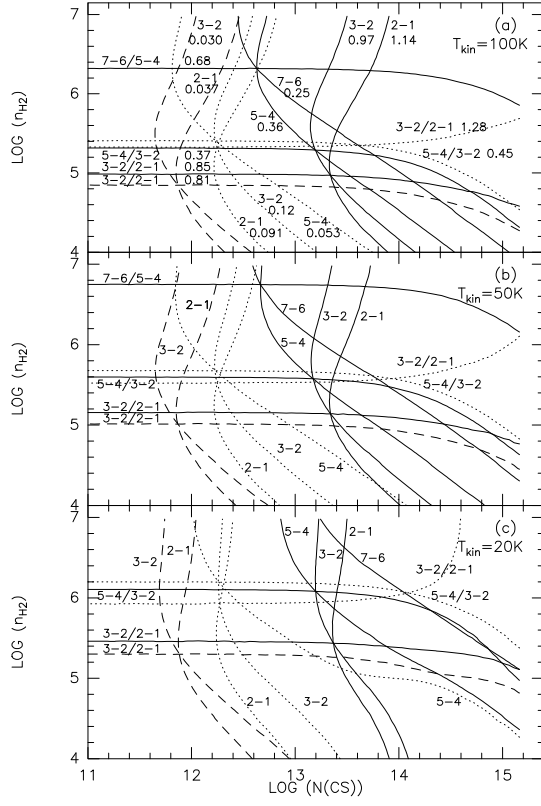


Fig. 9.— LVG calculations for CS (solid lines) and its rare isotopologues C^{34}S (dotted lines) and ^{13}CS (dashed lines) at $T_{\text{kin}} \sim 100 \text{ K}$ (a), $T_{\text{kin}} \sim 50 \text{ K}$ (b) and $T_{\text{kin}} \sim 20 \text{ K}$ (c).

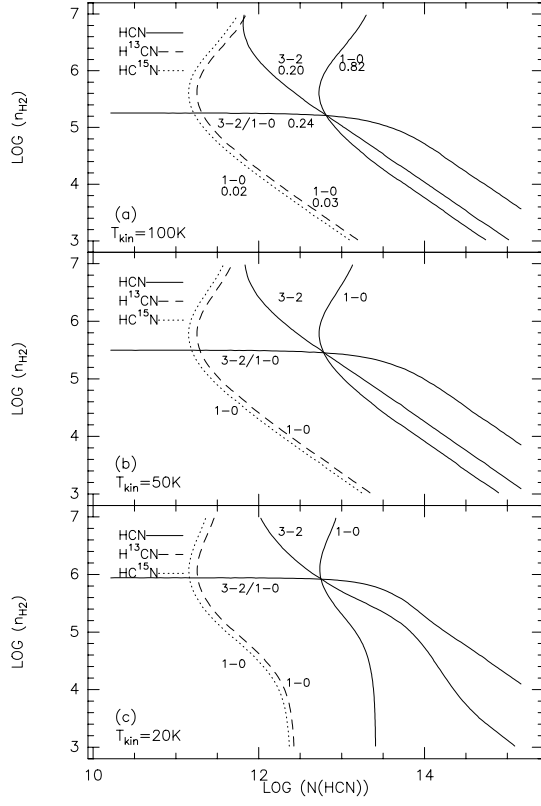


Fig. 10.— LVG calculations for HCN and its rare isotopologues H^{13}CN and HC^{15}N at $T_{\text{kin}} \sim 100\text{ K}$ (a), $T_{\text{kin}} \sim 50\text{ K}$ (b) and $T_{\text{kin}} \sim 20\text{ K}$ (c).

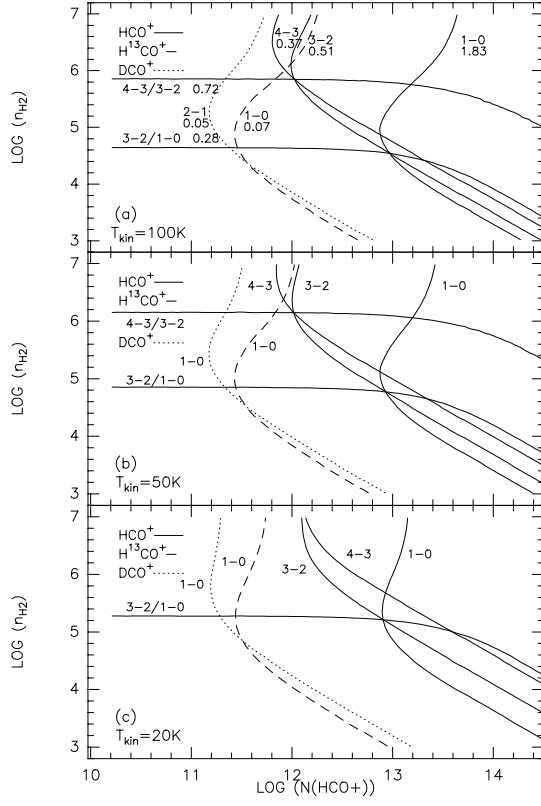


Fig. 11.— LVG calculations for HCO^+ and its rare isotopologues H^{13}CN and DCO^+ at $T_{\text{kin}} \sim 100 \text{ K}$ (a), $T_{\text{kin}} \sim 50 \text{ K}$ (b) and $T_{\text{kin}} \sim 20 \text{ K}$ (c). Note that for $T_{\text{kin}} = 20 \text{ K}$, no solution is found for the $J=4-3/J=3-2$ line intensity ratio.

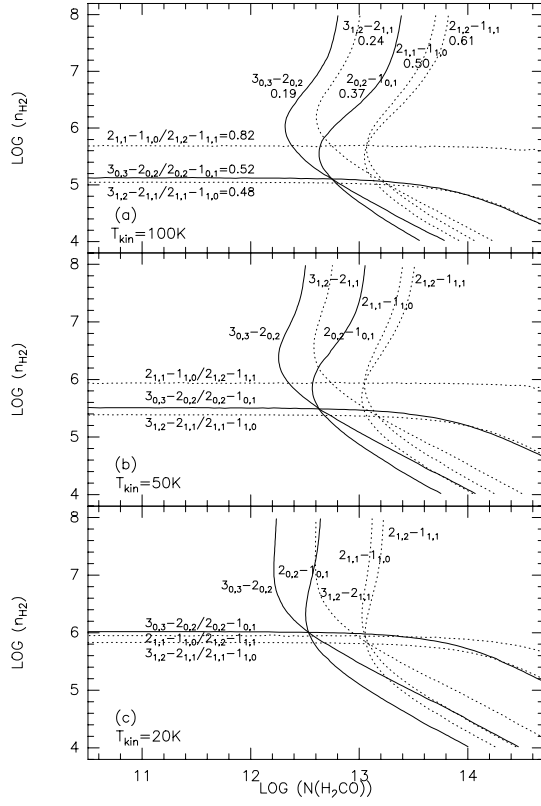


Fig. 12.— LVG calculations for para-H₂CO (indicated by solid lines) and ortho-H₂CO (dotted lines) at $T_{\text{kin}} = 100 \text{ K}$ (a), $T_{\text{kin}} = 50 \text{ K}$ (b) and $T_{\text{kin}} = 20 \text{ K}$ (c).

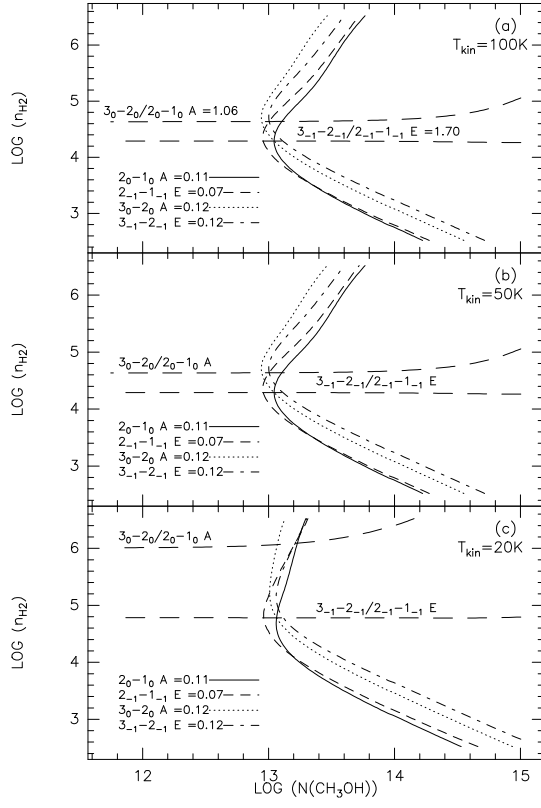


Fig. 13.— LVG calculations for CH_3OH at $T_{\text{kin}} \sim 100$ K (a), $T_{\text{kin}} \sim 50$ K (b) and $T_{\text{kin}} \sim 20$ K (c).